NOVEL MOTOR DRIVE DESIGN FOR A SWITCHED RELUCTANCE MACHINE BASED ELECTRIC VEHICLE PROPULSION SYSTEM

Peng Zhang

A Thesis

in

The Department

of

Electrical and Computer Engineering

Presented in Partial Fulfillment of the Requirements

for the Degree of Master of Applied Science at

Concordia University

Montréal, Québec, Canada

March 2010

Your file Votre référence
ISBN: 978-0-494-67242-6
Our file Notre référence
ISBN: 978-0-494-67242-6

ABSTRACT

Novel Motor Drive Design for a Switched Reluctance Machine Based Electric Vehicle Propulsion System

Peng Zhang

There exists an immense demand for efficient, robust, reliable, and cost-effective motors for propulsion systems in hybrid electric vehicles (HEVs) and plug-in hybrid electric vehicles (PHEVs). Due to the absence of windings on the rotor and excellent extended speed features, much attention has been recently drawn towards switched reluctance machine (SRM) based vehicle propulsion system. Although these advantages are beneficial, the inherently large torque ripple and highly nonlinear characteristics of the SRM presents significant challenges from the controller design standpoint. Hence, appropriate design of a dedicated control scheme is critical, so as to enhance the overall performance.

In order to achieve satisfactory control performance, the derivation of an accurate inductance model is essential. In this thesis, a "current saturation" approach is utilized, and the SRM magnetization characteristics are obtained from experimental results. Thereafter, the accuracy of the proposed method is discussed and verified by finite element analysis (FEA). In order to deal with SRM nonlinearities, this thesis introduces a finite approximation approach (Newton method) iteration computing algorithm. Based on the precise magnetic model, the optimal bus voltages are calculated, and are eventually stored in a meticulous look-up table. In order to engage high-speed switching control, a field programmable gate array (FPGA) is employed, and suitable simulation test results

are analyzed in detail. It was found that the overall output torque ripple was minimized considerably, using the proposed novel FPGA based "voltage-profile" control approach.

ACKNOWLEDGMENTS

The author would like to express his most sincere gratitude to his supervisor, Dr. Sheldon S. Williamson, for his patient and invaluable guidance, advice, friendship, and financial support throughout the Master's program.

The author also would like to appreciate the useful suggestions and helpful discussions of the other professors and colleagues in the P. D. Ziogas Power Electronics Laboratory. In particular, the author would like to express his sincere acknowledgement towards Dr. Pragasen Pillay for his dedicated help with regards to switched reluctance machines and his valuable comments from the bi-weekly research group meetings. The author would like to also deliver his gratitude towards Dr. Luiz A. C. Lopes and Mr. Joseph Woods for their notable advice. In addition, the author will never forget the valuable suggestions and enormous assistance from his colleague, Mr. Pablo A. Cassani.

Last, but not least, the author would like to express his sincere appreciation towards his parents. Without their constant encouragement and support, the author would hardly complete his thesis successfully.

TABLE OF CONTENTS

LIST OF FIGURES

LIST OF TABLES

LIST OF ACRONYMS

ADVISOR	Advanced Vehicle Simulator
ADC	Analog-to-Digital Conversion
BAS	Belt-Driven Alternator Starter
CCM	Continuous Conduction Mode
CV	Conventional Vehicle
DSPs	Digital Signal Processors
EMF	Electromotive Force
EV	Electric Vehicle
FCV	Fuel Cell Vehicle
FEA	Finite Elements Analysis
FPGA	Field Programmable Gate Array
GHG	Greenhouse Gas
HDL	Hardware Description Language
HEV	Hybrid Electric Vehicle
ICE	Internal Combustion Engine
IM	Induction Machine
IPM	Interior-Mounted Permanent Magnet
ISA	Integrated Starter Alternator
JTAG	Joint Test Action Group
LUT	Look-up Table
MEV	More Electric Vehicle

MMF	Magnetomotive Force
MSE	Mean Square Error
PMSM	Permanent Magnet Synchronous Machine
RMS	Root Mean Square
RPM	Revolutions per Minute
RTL	Register Transfer Level
SOC	State of Charge
SPM	Surface-Mounted Permanent Magnet
SRM	Switched Reluctance Machine
UDDS	Urban Dynamometer Driving Schedule
VHDL	VHSIC Hardware Description Language
XSG	Xilinx System Generator

LIST OF PRINCIPAL SYMBOLS

A	Aligned position
A-J	Parameters for voltage profile initialization
B	Flux density
δI	Current hysteresis bandwidth
E	Back-EMF
F	Switching Frequency
I_c	Copper current
I_i	Iron current
$I_{ph}/I_m/I_p$	Instantaneous phase current
I_{ref}	Reference phase current
J	Start of overlap
K	End of overlap
K_e/K_h	Constant parameter
L/ L_{ph}	Phase inductance
L_p	Parasitic inductance
λ	Flux linkage
L_c	Coupled inductance
ω_b	Base speed
ω_p	Boundary speed between the constant power region and the power falling region
ω_m	Angular velocity
P_e	Power losses due to the eddy current

P_h	Hysteresis losses
R/R_p	Phase resistance
R_{copper}	Copper resistance
R_{iron}	Iron resistance
R_m	Shunt resistor
R_p	Phase resistor
θ	Rotor position
θ_{off}	Turn off angle
θ_{on}	Turn on angle
T_{ph}	Phase torque
T-i-θ	Torque-angle-current
U	Unaligned position
V_b	Bus voltage
$V_p/V_{ph}/U_m$	Phase voltage
W'	Co-energy
$x/y/f(x)$	Variable applied in Newton Method

CHAPTER 1

INTRODUCTION

1.1 BACKGROUND

A growing dependence on petroleum, as well as heightened emission concerns of conventional vehicles (CVs), has launched an intense research focus on advanced vehicle architectures. Due to costly fuel and green house gases (GHG) emissions, CVs are hardly satisfying the future transportation market. Nowadays, in North America alone, almost two-thirds of petroleum is consumed by the transportation sector [1]. In addition, with rapid economic growth of developing countries, such as China and India, the dramatic increase of on-road automobiles in the next 15-20 years will aggravate the crisis of natural resources and environment [2]-[4]. Hence, much attention has been recently drawn towards electric vehicles (EVs), hybrid electric vehicles (HEVs), and plug-in hybrid electric vehicles (PHEVs). In order to improve the overall efficiency, reduce the cost and fuel consumption, the integrated starter alternator (ISA) is accepted as a good solution for HEV propulsion system, which is mounted on the same shaft with the internal combustion engine (ICE). As the name indicates, ISA integrates the functions of the starter and on-board generation, providing the higher efficiency of the entire propulsion system by allowing the motor work alone at low speed to generate the extra torque for acceleration and using the ICE alone at high speed to drive the traction motor as a alternator charge the battery and supply other electrical loads [5]. In addition, selection of a specific electric machine as well as an appropriate control strategy becomes

a crucial link from the point of view of overall system performance and efficiency [6]-[8]. Due to its robust construction, low cost, high efficiency, and excellent extend speed characteristics, the switched reluctance machine (SRM) is highly proposed and widely considered for HEV propulsion.

1.2 ISA FUNDAMENTALS

Instead of using two separate machines inside CVs, the ISA is used as an electric subsystem, with the function of engine starter and power generation for HEVs. This section will discuss the basic structure and functions of an ISA as well as introduce an ISA based power-system.

1.2.1 ISA ARCHITECTURE

The ISA machine is located in a position so as to replace the conventional AC generator (alternator), between the ICE and the mechanical transmission system. The ISA can be classified into two categories: belt-driven ISA (BAS) and crankshaft mounted ISA [5], [6]. The ISA is an electric subsystem, wherein the functions of the engine starter and on-board generator are fulfilled together. Instead of two separated electric machines, as is the case in CVs, the ISA eliminates the traditional starter and alternator as well as the flywheel, and implements all features into one electric machine. The comparison between the power system in CVs and the ISA power system are summarized in Fig. 1-1.

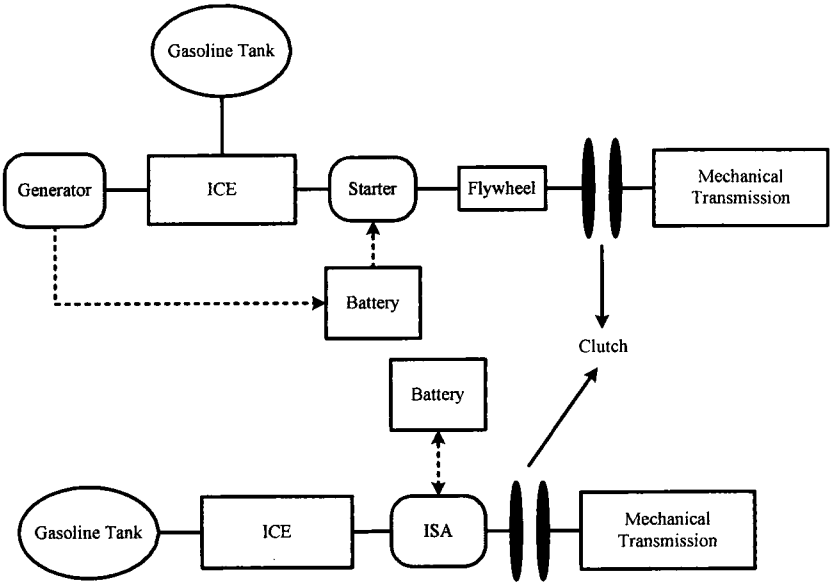

Fig. 1-1 Comparative layout of the traditional vehicular power system and the ISA power system

The ISA based electric drive subsystem consists mainly of an electric machine and a power electronic converter. Generally, the power electronic converter is comprised of a combination of a traction inverter and a bi-directional DC/DC converter [5]. The layout of critical components of the ISA subsystem is depicted in Fig. 1-2.

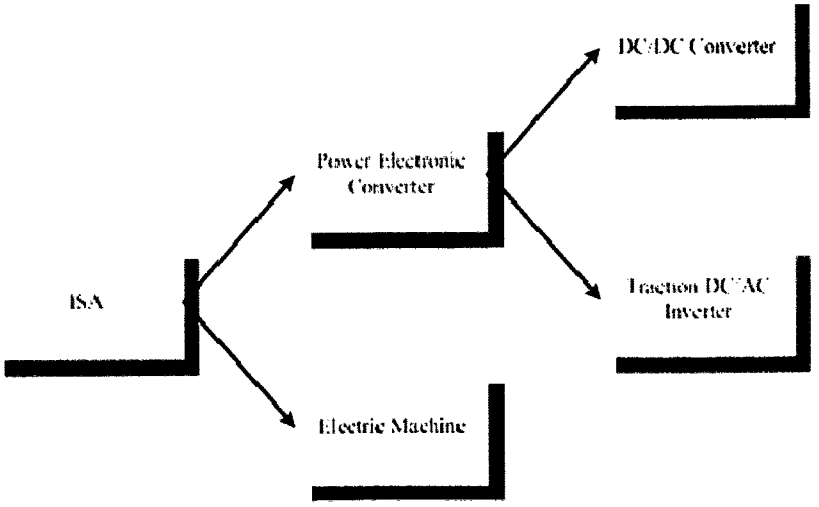

Fig. 1-2 Layout of the typical ISA subsystem

Not only is the ISA system expected to meet the large vehicular electric load requirement, but it also addresses the issue of fuel consumption. Besides, leading auto-manufacturers claim that their HEVs can save fuel as high as 40~50% [9], in urban driving conditions. Based on the ISA technology, the engine can be shut down when the vehicle is driven in a low speed region (or completely stopped). As a consequence, the ISA starts propelling the vehicle at a low speed or cold cranking, whereas the engine is on-line only when needed, such as low battery state of charge (SOC), highway driving, or turbo mode. Thus, improved fuel economy and low gas emissions are easily experienced. Furthermore, the ISA system is able to offer the vehicle stop/start, regenerative braking, cold cranking, and fast acceleration, for power enhancement in mild HEVs. The system works like a plug-in power system, which provides drive-line torque smoothing and on-board electrical power generation. This eventually results in a smoother ride and efficient on-board power generation [5].

1.2.2 ISA BASED MILD HEV LAYOUT

Based on a literature survey, it is found that the central control unit in an ISA power system can be adapted to dynamic load and state of charge (SOC) of the on-board battery pack [8]. However, since the ISA is isolated from other power sources, except the on-board battery pack, a stronger and more stable voltage output is necessary. Hence, an ultra-capacitor (UC) is preferably required to operate in parallel with the battery pack, so as to maintain smooth output voltage and enhance battery life.

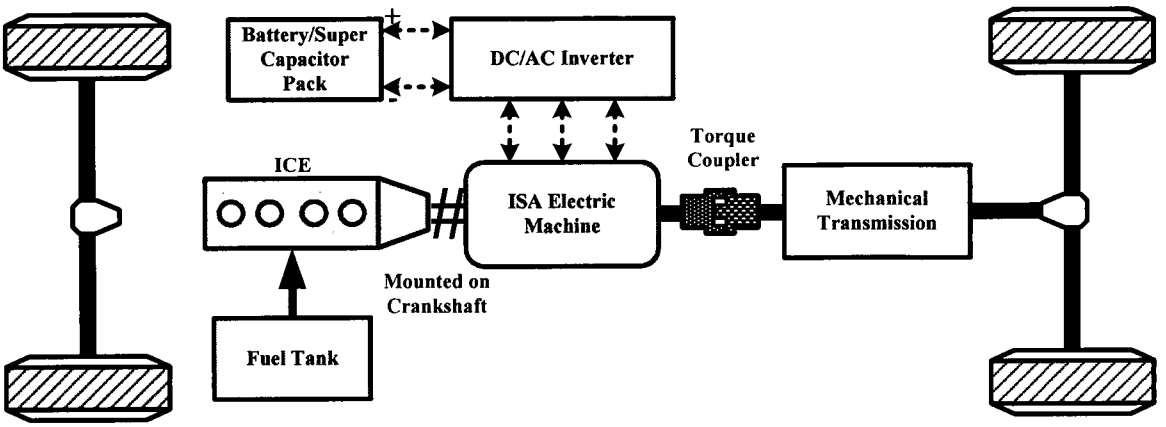

Fig. 1-3 Typical topology of an ISA based HEV drive train

Fig. 1-3 presents the schematic diagram of the ISA based HEV drive train system. Previous research has proven that a suitably sized battery/UC combination is a reliable and economical technique to offer repetitive ISA cranking power and accumulating energy from regenerative braking [10], [11].

1.2.3 ISA BASED ADVANCED VEHICLE POWER SYSTEM

In recent years, due to the trend of increasing vehicle electric loads, an advanced 42V PowerNet has been proposed, to maintain a high system voltage. In addition, a new concept of more electric vehicles (MEVs) is introduced into the automotive industry, so as to meet the inflated power requirement. In order to offer high reliability and enhanced safety, MEVs employ advanced power systems, substituting mechanical and hydraulic systems [12], [13]. Critical operating voltages for the aforementioned 42V PowerNet [12] are summarized in Fig. 1-4. As is clear, the maximum dynamic over voltage is essentially below 58V, including the instantaneous voltage. Hence, the voltage for system charging is set to 42V, which is the operating voltage for the entire electrical system, whenever the engine is running [12]. Due to the integration of mechanical and hydraulic systems into the electrical system, significant advantages that can be observed include enhanced

system performance and total efficiency as well as low cost manipulating procedure. Furthermore, low primary installed power decreases the overall system design complexity.

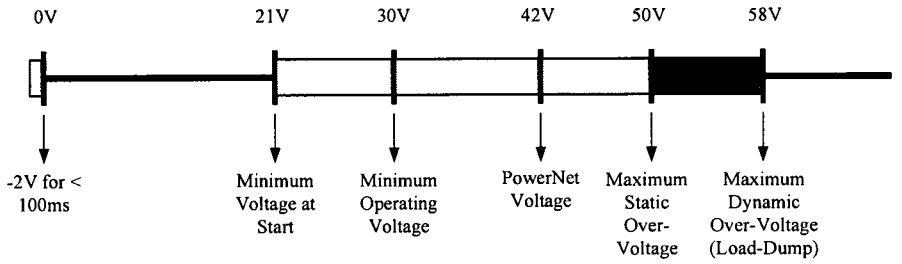

Fig. 1-4 Critical operating voltages for a 42V PowerNet

Literature survey reports that both the conventional 14V system as well as the proposed 42V system can be used initially as a hybrid (dual voltage) electric power system [12]-[14]. It is worth mentioning here that one of the leading breakthroughs includes the usage of the ISA with the redesigned 42V/14V dual voltage power system. The topology of a 42V/14V dual voltage power system, with dual batteries, is depicted in Fig. 1-5 (a). The power system topology of a single battery mode is shown in Fig. 1-5 (b). Fig 1-5 (c) presents the schematic diagram of a 42V/14V dual voltage, with dual stators and dual batteries [12].

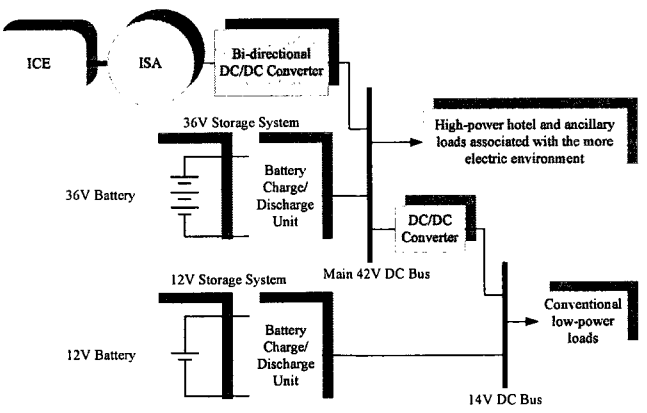

(a) 42V/14V dual voltage power system, with dual batteries

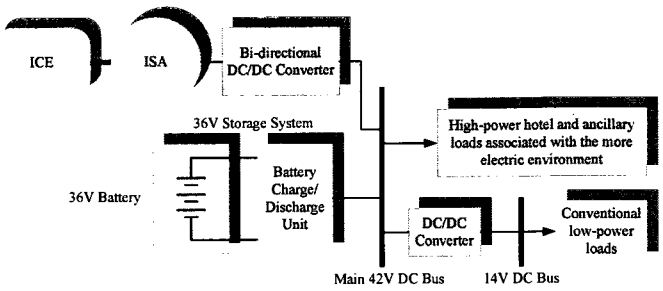

(b) 42V/14V dual voltage power system, with single battery

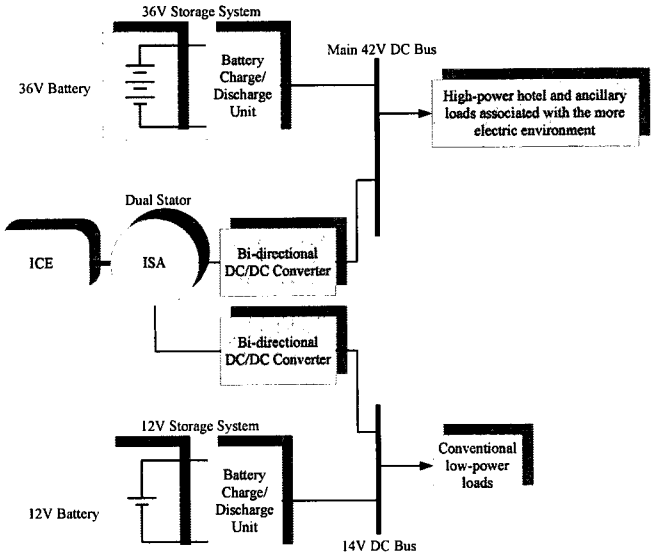

(c) 42V/14V dual voltage power system, with dual stators and dual batteries

Fig. 1-5 Schematic diagram of an ISA based 42V/14V dual voltage power system

As is seen in Fig. 1-5, the optimized voltage is set to 36V. Meanwhile, the low voltage is set to 12V [13], [14]. The main issue here is the usage of multiple batteries that highlights challenges such as increased cost, added weight, and space limitations. Improved vehicular functions, enhanced efficiency, and load driving ability are considered fair trade offs.

1.3 ISA MACHINE TOPOLOGIES: COMPARISON AND SELECTION

ISA based HEV traction system improvement through overall system performance optimization is also an important area of research. Electrical machine selection is a major criterion for faultless ISA operation. The prime ISA candidates include the induction machine (IM), permanent magnet synchronous machine (PMSM), and switched reluctance machine (SRM). Features of the different machine options are studied here. As aforementioned, the ISA is able to enhance fuel economy, provide high power efficiency, and driver friendly assistance. Furthermore, the ISA is not only capable of driving the ICE from idle speed (800 RPM) to maximum speed (more than 6000 RPM), but it can also offer the flexible management capability, by making use of non-sophisticated control strategies.

The IM is the most popular type of AC machine, which uses the popular principle of electromagnetic induction. An IM is made up of a three phase stator and a cage or wound rotor [15]. The characteristics of robust construction, low cost, and mature control techniques makes the IM a good candidate for ISA applications. Due to its operation principle, the stator current induces a magnetic field that interacts with the electromotive force (EMF) generated on the rotor side, which in turn yields resultant torque. Hence, the slip, known as the speed difference between the stator and rotor fields, needs to be taken care of [15]. As has been previously published in [15] and [16], slip at a given frequency is proportional to the loss in the rotor winding resistance. In terms of ISA operation, this scenario could lead to high machine losses during cold cranking or low speed operation. In order to reduce losses during cranking, rectangular stator windings as well as costly rotor copper coils could be employed. However, this would obviously mean high overall

cost. Moreover, along with increase in speed, the power capability of an IM decreases, especially during constant voltage operation [15], [16].

The PMSM benefits from inexistent filed-coil losses, and hence depicts high efficiency. From the architecture point of view, PMSMs can be classified as surface-mounted permanent magnet (SPM) or interior-mounted type permanent magnet (IPM). However, previous research [15] proves that trapezoidal SPM machines do not meet the voltage specifications in generation mode and wide-flux weakening performance at motoring mode, except when a specific DC/DC converter is used between the power inverter and the battery. Hence, the IPM architecture is considered as a more suitable candidate as an ISA electric machine. Due to dynamic features of driving time and road conditions, continuously changing power is demanded from the traction motor, in order to achieve variable speed operation [17]-[19]. However, the speed ratio for IPM is low, and a compromising approach is to optimize speed ratio via motor factor and power loss parameters. Another negative aspect of PMSMs is the high cost of permanent magnets, which are prone to irrecoverable demagnetization or loss of magnetic capability due to incorrect operation or accidents [17]-[20]. In order to protect the machine from demagnetization, a particular designed controller typically maintains motor speed in the safe range.

The switched reluctance machine (SRM) has double saliency structure, where the rotor poles and stator poles are different. In industry applications, it is categorized by the number of its stator and rotor pole combination, as 6/4, 8/6, and 12/8. An SRM inherently depicts excellent wide speed range operation, robust construction, low cost, and high starting torque, which makes it very attractive as an ISA. Moreover, the direction of

applied phase current is independent of direction of rotation, due to the absence of rotor windings [15]. From the point of view of operation, the reluctance torque is produced when the poles of the rotor and stator tend to be aligned, in order to maximize flux linkage. To obtain continuous mechanical rotation, each phase, consisting of two opposite poles pairs, is energized in an appropriate sequence. Due to frequent power injection, the torque ripple is found to be unexpectedly high. Furthermore, acoustic noise, vibrations, and high non-linearity gives rise to higher control complexity [21]-[23]. Thus, the parameters of applied phase current and switching angle rely highly on the feedback of accurate rotor position. Hence, a position sensor is included in the system. It must be pointed out here that copper losses are dominant at low speeds, while iron losses are dominant at high speeds. The comparison of the critical characteristics of the three machine topologies is as summarized in Table 1-1.

Table 1-1 Comparison of different ISA electric machines

Electric machine	IM	PMSM(IPM)	SRM
Efficiency	Low	Highest	High
Speed range	Wide	Narrow	Widest
Control	Complex	Complex	Easy
Torque ripple/noise	Low	Low	High
Cost	High	Highest	Low
Maintenance	High	Low	Low
Power density	High	Highest	Higher
Demagnetization	No	Yes (potential)	No

It is obvious that if an IM needs to be used as an ISA traction motor, it has to be oversized, in order to obtain satisfactory performance. This is due to the relatively low power density of an IM, which contributes towards increased vehicle mass. Furthermore, low efficiency is also an additional issue. The major drawback of an IPM is its narrow

speed range. High cost of magnetic materials and possible demagnetization pose additional challenges. On the other hand, SRMs depict excellent speed range operation. However, the high torque ripple, vibration, and acoustic noise need to be appropriately addressed.

1.4 THESIS OBJECTIVE

Based on the preceding discussion, SRM proves to be a prime candidate for HEV ISA application. The principal objectives of this thesis is to address the issues related to the highly non-linear SRM characteristics as well as to design an appropriate digital controller to minimize torque ripples in the complete speed range. Instead of typically adjusting the phase current and turn-on/off angles in real-time, a novel more advanced off-line strategy, using an optimized voltage profile technique is proposed. More importantly, the critical non-linear features are exclusively included in the calculations.

Obtaining a precise SRM inductance model is critical, in order to maintain excellent controller performance. A current saturation method is proposed to obtain the magnetization characteristic, and the accuracy of the results is verified by a 2-D finite element analysis (FEA) approach. According to the obtained inductance profile, the proposed voltage profile algorithm is applied to calculate the optimized voltage for each rotor position, over the entire speed range. Finally, a *Xilinx Virtex II Pro* field programmable gate array (FPGA) is employed as a controller, to process the voltage profile. The voltage profile is constructed using a look-up table, in terms of rotor position and speed. Furthermore, the *Xilinx* system generator (XSG), based on MATLAB/Simulink, is used as a development environment. The results obtained by JATG based hardware co-simulation are also presented and analyzed in the thesis.

1.5 THESIS OUTLINE

The contents of this thesis are organized into 6 chapters. Chapter 1 introduces a brief background of HEVs and the structure of an ISA power system. In addition, different electric machine topologies are considered for ISA applications. From among the various machine topologies, the SRM is selected for the purpose of further investigation, due to its intrinsically favorable characteristics.

Chapter 2 introduces the basic principle of operation of an SRM. The basic functionalities and non-linear characteristics of SRMs are also introduced. Conventional control techniques for torque ripple minimization are explained and the limitations of each approach are highlighted.

Chapter 3 introduces a novel procedure to obtain the SRM inductance profile. The advantages of the proposed method are highlighted and compared to conventional approaches, including the method to overcome the error introduced by dominant power losses. Finally, the accuracy of the proposed technique is verified by comparing the obtained results with those obtained by means of 2-D FEA.

Chapter 4 introduces the finite approximation approach based voltage profiling algorithm (Newton method). Based on the obtained inductance model, the iteration calculation is executed, to seek the corresponding voltage profile, with minimal torque ripple production. The comprehensive calculation procedure is presented and discussed, based on the computation of parameters for voltage-profile initialization and pulse-width modulation (PWM) cycle distribution for memory saving.

Chapter 5 provides an introduction to the *Xilinx Virtex II Pro* FPGA, which is used as the central controller, to drive the SRM. In addition, the XSG development tool is

studied in detail, in order to perform the FPGA based experiment. Thus, it is possible to obtain all the summarized results through the Joint Test Action Group (JTAG) hardware co-simulation. From the controller design point of view, the scheme of the entire system layout is depicted. Thereafter, each critical component in the system is explored and their main functions are discussed. With regards to experimental tests, the resultant torque-ripple, yielded from popular conventional techniques and the proposed voltage profiling technique are compared and contrasted. Thereafter, the results are presented by operating the SRM at low speed, high speed, and ultra-high speed, using the developed control technique. Thus, the performance of the developed controller is evaluated by observing the torque ripple over the entire speed range. An additional test, using the urban dynamometer driving schedule (UDDS), is conducted, in order to replicate actual vehicle driving load conditions and to check system dynamic response ability as well as overall motor/controller efficiency.

Chapter 6 summarizes the tests and studies performed in this thesis, by means of expositing the essentials. Possible future research topics are suggested based on the accomplished results.

CHAPTER 2

SRM FUNDAMENTALS AND REVIEW OF CONVENTIONAL CONTROL STRATEGIES

2.1 INTRODUCTION

Due to its robust construction, low cost, low maintenance, high efficiency, and high starting torque, the SRM has attracted immense interest and has been highly proposed for HEV propulsion. Compared to IMs and PMSMs, SRMs depict excellent extended speed range. Furthermore, the simple and robust construction of an SRM yields a low-cost solution. However, the down side of an SRM includes the inherent high torque ripple production. Moreover, SRMs inherently depict highly non-linear characteristics, whereby phase current is highly dependent on the injected current and instantaneous rotor position.

In order to address the high torque ripple issue and to improve overall performance, the overall mechanical structure needs to be improved. This approach may be accompanied with exposure to increased design complexity and supplementary expenses. Alternatively, an elaborately designed controller and motor drive could be employed [24]-[26]. This thesis primarily focuses on the control strategy for torque ripple minimization for an 8/6 SRM.

The fundamental principle of SRM operation is presented in this chapter. In addition, the mathematical model for torque production as well as electromagnetic

characteristics is also introduced. Conventional control strategies are reviewed and the limitations of each method are discussed.

2.2 SRM FUNDAMENTALS

In this section, a basic 8/6 SRM is introduced in terms of its topology and principle of operation. The main focus is placed on critical mathematical model derivation, electromagnetic characteristics, and overall torque production.

2.2.1 SRM TOPOLOGY

The SRM possesses a double salient structure, with different number of poles on the rotor and the stator. In this thesis, an 8/6 SRM is considered, having 8 poles on the stator and 6 poles on the rotor, as shown in Fig 2-1.

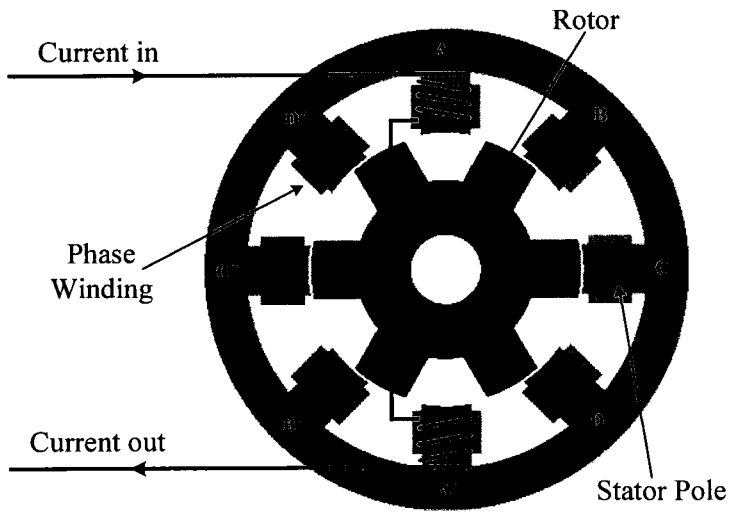

Fig. 2-1 Topology of an 8/6 SRM

The rotor is simply a stack of laminated salient poles, without phase coils or permanent magnets. Hence, the electromagnetic field is only generated from the stator side. Thus, the SRM does not suffer from demagnetization issues, like in case of PMSMs.

The 8/6 SRM has even number of stator poles, which divides into 2 pole pairs, to form 1 electrical phase. Thus, the 8/6 SRM is considered as a four-phase electric machine, known as AA', BB', CC', and DD', as is clear in Fig 2-1. To better understand the SRM operation, consider a current pulse applied to AA'. Consequently, a magneto-motive force (MMF) is produced, which develops a magnetic flux, which tends to align the stator and rotor poles. Hence, mechanical rotation is gained due to a reluctance torque [27], [28].

2.2.2 Principle of Operation of an SRM

To achieve continuous mechanical rotation, the different phases need to be energized independently, in an appropriate sequence, in order that the rotor is constantly pulled into the aligned position by the activated phase. A reluctance torque is duly produced, due to the flux linkage of the stator and rotor poles. Meanwhile, the flux across the air-gap induces minimal torque on the rotor [28]. However, the produced torque cannot solely align the rotor and stator poles. If the active phase is continuously injected with power, the rotor will essentially be locked into the aligned position [27], [28]. Thus, it is obvious that de-energizing of the activated phase has to be executed before activating the next phase in sequence, in order to minimize torque conflict. Fig. 2-2 [27] depicts the variation of inductance and phase voltage between the aligned and unaligned positions.

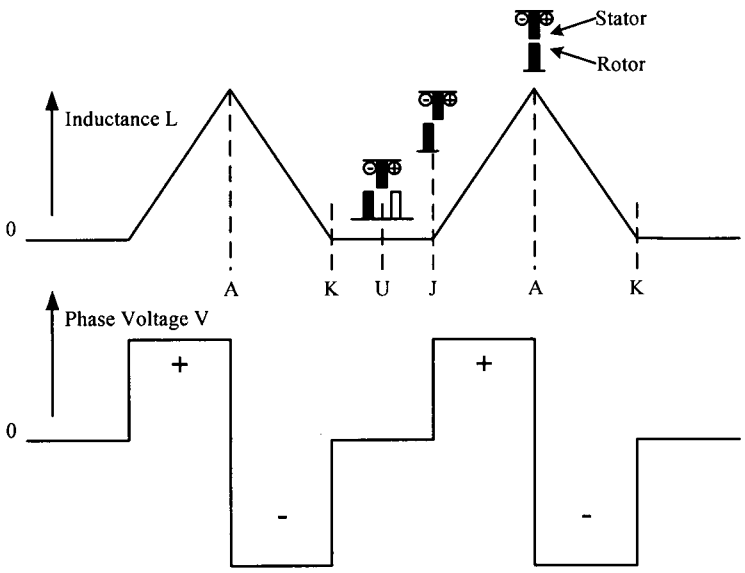

Fig. 2-2 Basic operation of SRM under constant current (A = aligned position, U = unaligned position, J = start of overlap, K = end of overlap)

Based to Faraday's law, the negative voltage is needed at the end of each stroke, in order to restore the flux-linkage to zero [27]. The amplitude of the negative voltage must be larger than the amplitude of the positive voltage, in order to reduce the flux and phase current to zero as quickly as possible, according to Fig. 2-2. This scenario corresponds to the rotor positions of A-K and J-A, respectively. Additional negative voltage is also acquired for regulating the torque. This situation avoids flux-linkage overflow beyond the aligned position. At the same time, it also forms the negative torque pulse [28]. A typical SRM motor drive is required to provide unidirectional current and bidirectional voltage. One phase of a classic SRM drive is shown in Fig. 2-3, whereby two switches and two diodes represent one phase. In this drive arrangement, switches S_1 and S_2 turn on and off at the same time. When the switches are on, the bus voltage V_b is applied across the phase winding and phase voltage V_p is equal to V_b; when the switches

are off, the current passes through the phase winding via the freewheeling diodes D_1 and D_2, and V_p is equal to $-V_b$.

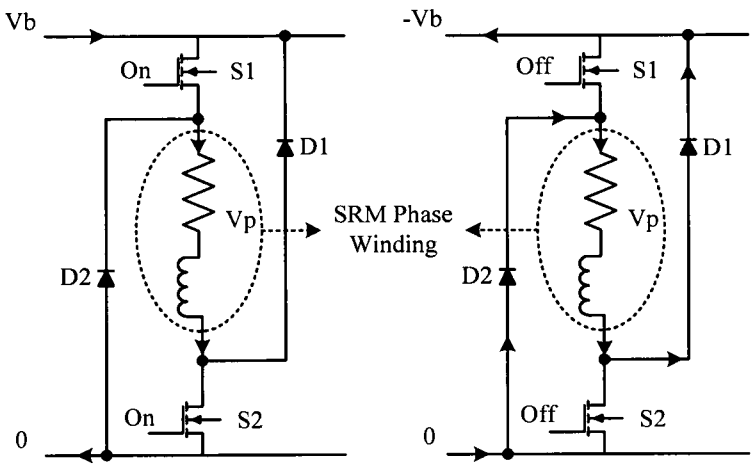

Fig. 2-3 One phase of a classic SRM drive

Due to its extremely non-linear characteristic, the solution of the mathematical model of an SRM is relatively difficult. The instantaneous voltage across the terminal of one phase of an SRM is comprised of copper resistance and flux-linkage across that specific phase winding. The electrical model of an SRM can be summarized as:

$$V_{ph} = RI_{ph} + L(\theta, I_{ph})\frac{dI_{ph}}{dt} + \omega_m I_{ph}\frac{dL(\theta, I_{ph})}{d\theta} \tag{2-1}$$

Here, V_{ph} is the phase voltage, R is the estimated phase resistance, I_{ph} is the instantaneous phase current, L is the inductance, θ is the rotor position, and ω_m is the angular velocity. The term $\omega_m I_{ph} \cdot dL(\theta, I_{ph})/d\theta$ represents back-EMF, which is proportional to angular speed and phase current. In addition, the flux linkage in each phase is calculated by integrating the overall difference between the phase voltage and the voltage drop due to phase resistance in the winding:

$$\lambda(t) = \int_0^t (U_{ph} - I_{ph}R)dt \tag{2-2}$$

Here, U_{ph} is the phase voltage, I_{ph} is the calculated phase current, and R is the estimated copper resistance. The flux for one rotor position is obtained by integrating the inductive voltage over a time period. The same procedure is repeated to obtain the flux profile for all rotor positions. Hence, the inductance value can be estimated using a derivative of the flux over phase current, and can be expressed as shown in (2-3):

$$L(I_{ph}\theta) = \frac{\partial \lambda(I_{ph}\theta)}{\partial I_{ph}} \tag{2-3}$$

Electrical torque is produced while one phase is energized and the magnetic circuit tends to approach the position with minimal reluctance, whereby the rotor pole is aligned with the excited stator pole, while phase inductance value keeps rising. Maximum torque is produced in the high current saturation area. Therefore, the torque ripple is high, due to frequent injection of current into different phases. The rate of change of magnetically stored energy at any instant is summarized as [27]:

$$\frac{d}{dt}(\frac{1}{2}LI_{ph}^2) = \frac{1}{2}I_{ph}^2\frac{dL}{dt} + LI_{ph}\frac{dI_{ph}}{dt} = \frac{1}{2}I_{ph}^2\omega_m\frac{dL}{d\theta} + LI_{ph}\frac{dI_{ph}}{dt} \tag{2-4}$$

It is clear that power can be obtained by multiplying torque with corresponding angular velocity. Hence, the produced phase torque can be obtained using:

$$T_{ph} = \frac{P}{\omega_m} = V_{ph}I_{ph} - I_{ph}^2R - \frac{d(\frac{1}{2}LI_{ph}^2)}{dt} = \frac{1}{2}I_{ph}^2\frac{dL}{d\theta} \tag{2-5}$$

Here, T_{ph} represents the phase torque. It is worth mentioning here that this technique of obtaining phase torque is somewhat inaccurate, due to the high saturation of SRM winding. Thus, the phase current is highly dependent on both the rotor position as well as phase inductance. In this case, in order to calculate torque production by each phase, the magnetic co-energy information is utilized, which can be obtained through the integration

of flux linkage over phase current. Equation (2-6) represents the relationship between torque and flux linkage.

$$T_{ph}(I_{ph},\theta)=\frac{\partial}{\partial\theta}W'(I_{ph},\theta)=\frac{\partial}{\partial\theta}[\int_0^{I_{ph}}\lambda(I_{ph},\theta)dI_{ph}] \tag{2-6}$$

W' represents co-energy, in (2-6). Thus, the magnetic characteristic of an SRM can be obtained. Consequently, the produced electrical torque as well as torque ripple can be accurately estimated and analyzed. The comparison of electromagnetic torque between an ideal case and a real case is shown in Fig. 2-4.

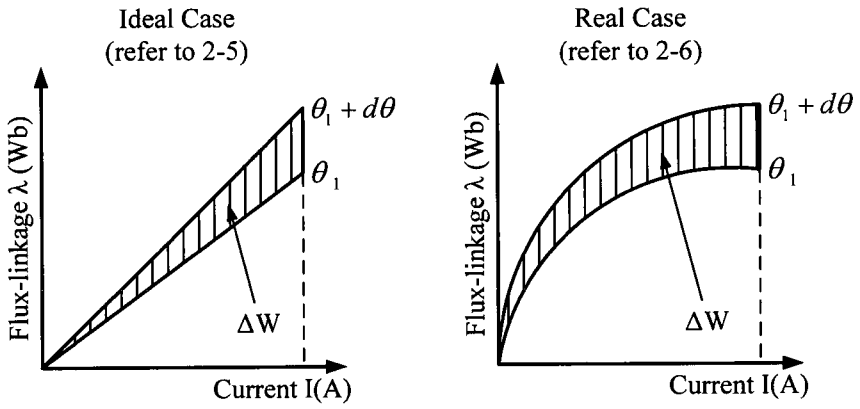

Fig. 2-4 Comparison of estimated electromagnetic torque

Based on the SRM torque-speed characteristics, shown in Fig. 2-5, three different speed operation regions can be noticed. As aforementioned, wide range of speed operation is a major advantage of SRMs over other machine types. The first region is known as the constant torque region, whereby maximum current is applied to the motor at rated voltage. The torque remains constant and the achieved maximum speed is called base speed (ω_b). In this region, since the speed is low, the toque is able to be controlled by regulating the current and adjusting the turn-on and turn-off times of the drive switches. When the motor speed rises beyond base speed, in the second operation region, the torque starts reducing and is inversely proportional to the angular velocity. In this

region, motor power remains constant. Thus, this region is also known as the constant power region. It is interesting to note that the rate of increase in back-EMF is less than that of angular velocity. This is because current decreases with angular velocity; and hence, $d\lambda/d\theta$ reduces [27].

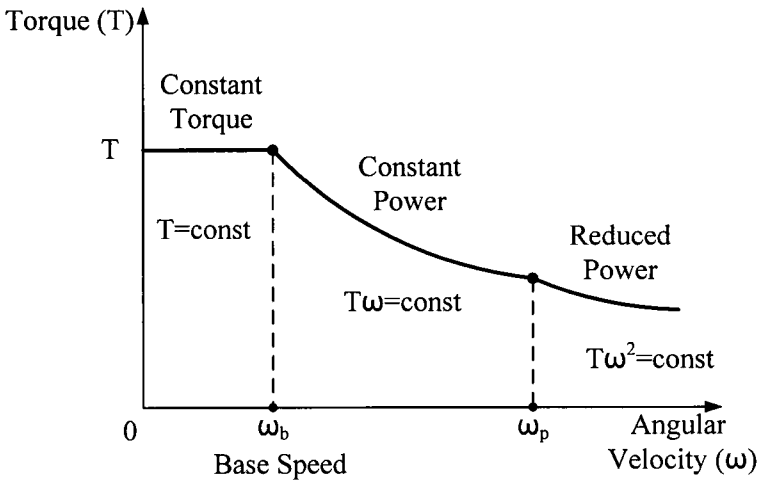

Fig. 2-5 SRM torque-speed characteristics (motoring mode)

In the final speed-torque envelope, the power is proportional to the product of torque and square of angular velocity. As is clear from Fig. 2-5, the decrease in torque is not compensated by increase in angular velocity, and hence, power no longer remains constant. On the contrary, power starts to reduce. In terms of control complexity, this region represents an overlap between turn-on and turn-off angles, due to which resultant flux does not return to zero at the end of each phase operation. This gives rise to a continuous conduction mode (CCM) [27], [28]. In this case, the phase winding continues to get saturated and angular velocity goes greater than ω_p.

2.3 REVIEW OF CONVENTIONAL CONTROL STRATEGIES FOR SRM TORQUE RIPPLE MINIMIZATION

In this section, two conventional control strategies are summarized. These strategies include the popular current profile based control technique and the fuzzy logic based control technique. This section introduces the algorithm followed by each control technique and major drawbacks.

2.3.1 CURRENT PROFILE BASED CONTROL

A popular torque ripple minimization method is proposed in [29], which is based on optimum profiling of the phase currents, during an extended overlapping conduction period of two phases. Instead of using conventional time-averaged torque control, this control method is based on instantaneous torque information. The approach uses the torque-angle-current *(T-i-θ)* characteristics stored in a tabular form, in order that the optimum phase current be determined by both the torque requirement and position measurement [20], [30]. The *(T-i-θ)* characteristics can also be determined offline, by conducting static tests on the motor. While magnetic non-linearity is neglected, the *T-i-θ* characteristics curves can also be obtained from the self-inductance data. In this method, the equation of phase voltage calculation is referred to 2-1. Since back EMF is a function of speed and inductance slope, the derivative of the above equation can be written as [29]:

$$\frac{dI_{ph}}{dt} = \frac{V_{ph} - E}{L} + \exp(-\frac{Rt}{L}) \tag{2-7}$$

Here, E is the back-EMF. The above functions limit the performance of this torque ripple minimization technique only in certain speed ranges [29]. Moreover, the phase current

can be managed within desired limits by PWM control, which is a fixed-frequency, varying duty-cycle PWM control. The real current is sensed and fed back as an error signal, after which it is compared with the reference current, and passed through a PI controller, to generate the desired duty-cycle for the active phases. The overall control block diagram is shown in Fig. 2-6 [29].

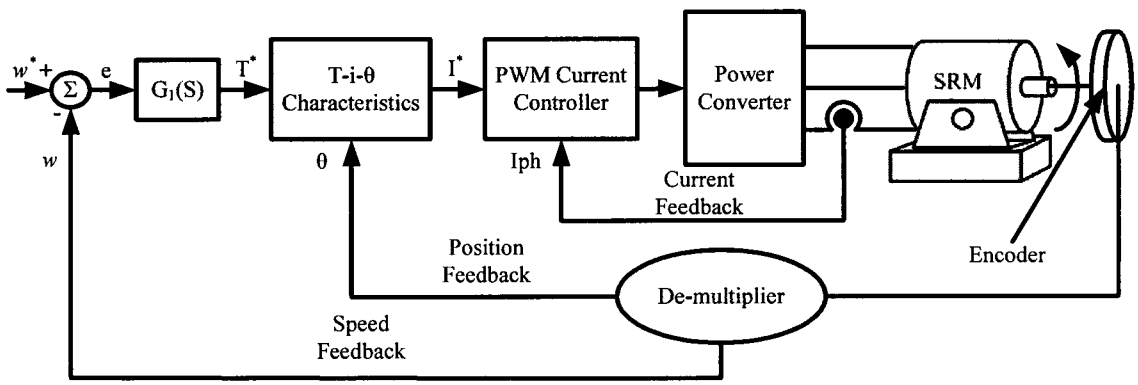

Fig. 2-6 Block diagram of a typical current-profile based controller

This method presents a current profile control strategy, wherein the current follows a contour for constant-torque production. It is found through pertinent literature that at base speed, this method yields torque ripples in the order of about 10% [29]. However, due to the limitations of DC bus voltage, the controller is unable to profile the current exactly at high speeds. The peak torque production is then handled by controlling the conduction angle, while the motor operates in the extended-speed/constant power region. In this speed range, the torque ripples are even higher than at low speeds, which is highly undesirable for automotive propulsion applications. Therefore, this control approach is not good enough for the SRM torque ripple minimization over the entire speed range.

2.3.2 FUZZY LOGIC BASED CONTROL

Due to the highly non-linear nature of the SRM inductance profile, non-linear control mode using fuzzy logic is highly proposed in recent literature. It is found that, since classic controllers normally do not compensate for the system delay, they contribute significantly towards the torque ripple content [30]. The method proposed in [31] presents a torque controller by regulating the phase reference current and adjusting turn-on as well as turn-off angles, using fuzzy logic control. This method reduces the instantaneous torque ripple by accurately tracking torque command.

Typically, if a current hysteresis-band controller is used in each phase, 4 motor parameters are controllable, namely reference phase current, I_{ref}, turn-on angle, θ_{on}, turn-off angle, θ_{off}, and current hysteresis bandwidth, δI [31]-[33]. Since these parameters are highly non-linear, the first 3 need to be adjusted in real time, in order that they indirectly regulate the torque in each phase. The final parameter is set as constant, for a specific application, as a trade-off between switching losses and current control accuracy [31], [32]. Therefore, the torque ripple minimization under this specific approach is based on the principle of indirect torque control, in real time [31].

A fuzzy logic controller is designed with specific θ_{on} and θ_{off}. The input of the controller is the rotor speed, obtained by a feedback speed sensor. The output comprises of the fuzzy degree of membership. The switching angle variable is divided into many fuzzy regions; each region is assigned a fuzzy membership function, with triangular or trapezoidal shapes [31]-[33]. The control block diagram for the overall system is shown in Fig. 2-7 [31].

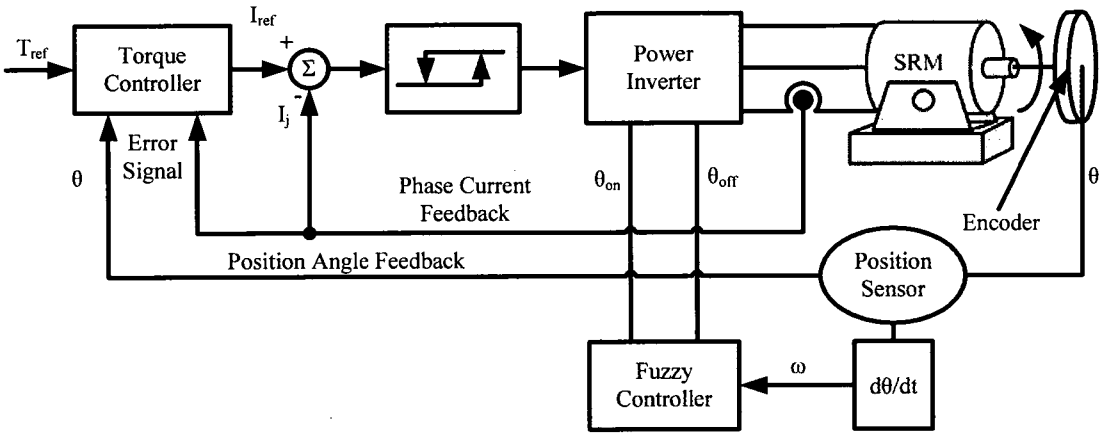

Fig. 2-7 Block diagram of a typical non-linear fuzzy-logic controller

Using this method, the torque ripple reduces to a satisfactory level of about 5%, at 300 rpm. However, torque ripples increase to about 20% at 1500 rpm [31]. The reason for this vast difference is the same as was highlighted in the current profiling method, whereby the instantaneous phase current is unable to follow the desired reference current in the high-speed region, due to the significant rise of phase voltage [31]. Therefore, this method is also not appropriate for control over the entire speed range, as demanded by electric traction applications.

2.4 SUMMARY

This chapter summarized the topology of an SRM and its principle operation. The initial part of the chapter introduced the structure of an 8/6 SRM and an electrical model was derived, whereby it was observed that the SRM can rotate due to the production of a reluctance torque. From the point of view of principle of operation, discussions were mainly focused on four topics: the basic operating principle of an SRM, the classic SRM drive topology (per phase), the calculation of produced torque, and the SRM torque-speed characteristic. To ensure continuous rotation, de-energizing the phase is necessary, when

phase inductance starts to decrease. Moreover, to reduce flux and current to zero as quickly as possible, additional negative voltage is applied, corresponding to the falling part of phase inductance. Therefore, two switches and two diodes are required per phase, to allow unidirectional current and bidirectional voltage operation. In view of phase winding saturation, produced torque is calculated using co-energy information. Phase current is highly dependent on rotor position and phase inductance. The SRM torque-speed characteristic summarizes its excellent wide speed range of operation, and also suggests that the conventional control strategy is not suitable at high speeds.

In addition, this chapter also reviewed two conventional torque ripple minimization control strategies. However, for both strategies, test results from literature show that resultant torque ripples are high, especially at high speeds. The major limitation of both popular classic control strategies is that current becomes difficult to regulate accurately at high speeds, since there exists a dramatic increase in back-EMF. In addition, the turn on/off angles cannot trigger the corresponding switches on time due to discrepancy with the rapidly varying flux. Therefore, this thesis proposes a novel approach to deal with the high non-linearity and torque ripples in the entire speed range.

CHAPTER 3

NOVEL SRM INDUCTANCE MEASUREMENT TECHNIQUE

3.1 INTRODUCTION

As aforementioned, the significant disadvantages of SRMs include acoustic noise, vibrations, and high torque ripple production. Moreover, SRMs inherently depict highly non-linear characteristics, whereby its phase inductance is highly dependent on the phase current and rotor position. Hence, it is imperative that accurate SRM modeling is performed, in order to achieve improved overall control performance.

Due to double saliency in its structure and magnetic saturation during increase in winding current, the SRM is complicated to model accurately [34]. Normally, the performance of SRM is studied through its magnetization curves for different rotor positions and applied phase currents. The results can be obtained by experimental measurements or calculated from the SRM model, using finite element analysis [35], [36]. In general, in order to measure the flux linked in one phase of the SRM, the rotor is blocked in a certain position (normally, starting from the unaligned position), and a pulse voltage is applied in one phase. The measurement is repeated for different rotor positions, to represent the flux curve for variety of phase currents, in 1 electric period. It is verified from previous related literature that the rates of increase and decrease of flux is different, which means the iron (core) losses and copper losses need to be taken care of [37].

A 2-D Finite Element Analysis (FEA) is widely accepted for SRM magnetization characteristics and performance evaluation/analysis. It is used as a numerical analytical

tool to study the flux curve in each stator pole winding, phase inductance, and developed torque [36], [38]. Although the FEA method can offer more accuracy compared to the standard analytical method [38], it needs more prior tests and exact geometrical parameters, in order to model the motor. However, it presents a robust method to verify the obtained experimental results.

This chapter proposes a novel method to measure the inductance profile of the SRM. Furthermore, the iron losses and copper losses are considered during measurement. Moreover, specific devices such as torque transducers and flux sensors are not deemed necessary. The proposed method makes use of a DC voltage in one phase of the SRM, with its rotor blocked in a fixed position. The asymmetry function generator connects with a switch as a gate control signal. The magnetic curve can be obtained by repeating this process for a variety of rotor positions. An alternate method involves rotating the rotor at a very low speed, while a fixed current can be applied on each phase of the motor. Finally, the duplicated procedure is utilized for different current levels. Since the setup for this method is more complicated than the former, it can be accepted as an alternative method.

3.2 Review of Conventional Inductance-Profile Measurement Techniques

This section introduces the conventional methods to measure the inductance profile of an SRM. The experimental procedures are discussed for each of them and their respective advantages and disadvantages are studied.

3.2.1 AC/DC TEST METHOD

The experimental circuit setup, depicted in Fig. 3-1, suggests that the instantaneous value of the phase inductance is based on the measurement of the instantaneous value of phase current [39]. When S1 is on, S2 is off, AC voltage is converted to DC, through a rectifier, and the capacitor is charged until S1 is off and S2 is on. The capacitor works as a DC voltage source, feeding the SRM phase winding. Based on the AC/DC test setup, an external resistor is necessary to obtain the current through the phase winding of the motor. The applied digital oscilloscope is used to obtain the voltage throughout the phase winding and the voltage of the measured resistor, in order to calculate the phase current. Here, R_m is the shunt resistor, R_p is phase resistor, and L_p is phase inductance. Since the phase voltage recorded by the oscilloscope is not the pure inductive voltage, the resistive voltage should be eliminated before integration, to obtain the flux. The function is referred to equation 2-2 in previous chapter. The flux is gained through integrating the inductive voltage over time. The aligned as well as unaligned position of the motor is measured to obtain the waveform for maximum and minimum phase current variation tendency. The obtained phase current can be used for the calculation of flux (as a function of current) boundary. Magnetic curves for other rotor positions in 1 electric period are determined by following by the same procedure, after which the inductance profile can be calculated by the function 2-3 discussed in previous chapter.

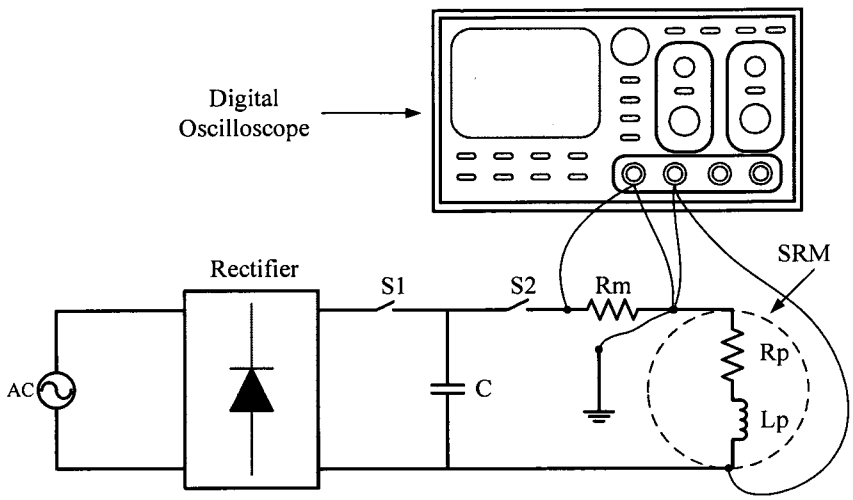

Fig. 3-1 Experimental layout of the AC/DC test method

Due to its simple experimental setup, the AC/DC test has a major benefit in that the error introduced by the devices can be reduced to a minimal level. Moreover, the value of the capacitor can be maintained at a desired level to control the output DC voltage. This, in turn, ensures that the phase current will not be large enough so as to damage the SRM.

However, careful attention should be given to critical disadvantages of such a setup, which directly affects the accuracy of experimental results. Firstly, the harmonics introduced by the AC source will be amplified throughout the numerical calculation. In addition, the included noise in the recorded phase voltage is hard to be filtered due to the varied frequencies of the harmonic error. Secondly, the duty ratio of the switches should be controlled in order that the phase current achieves its maximum value, otherwise the imprecise flux value could affect the maximum inductance value. Such a practice is highly unreliable, since the data of the developed torque will be estimated incorrectly. Moreover, the core losses contain both eddy current losses as well as hysteresis losses, and are based on the variation of the magnetic field in the iron. Eventually, the error

introduced by machine losses will be increased the converted AC/DC voltage, which cannot be neglected.

3.2.2 DIRECT DC TEST METHOD

The direct DC test method applies a pulse voltage on one phase of the SRM, with its rotor blocked in a fixed position. The phase resistance, R_p, is pre-measured, after which the inductance can be estimated directly from the measured voltage and current. It must be pointed out here that flux calculation is not necessary. To build the whole system, a single phase inverter, including 2 MOSFET switches and 2 diodes, is connected with one phase of the SRM. The experimental setup is shown in Fig. 3-2 [40]. The voltmeter and ammeter are parallel and series connected with the phase, respectively. A gate drive circuit provides the MOSFET control signals: when they are on, the DC source directly supplies power to the phase winding, in order that the phase current increases; when they are off, the phase current, through the 2 diodes, feeds back power to the DC source. The same procedure is repeated to obtain the current curve in different rotor positions, after which, the inductance profile is calculated directly from the measured current value.

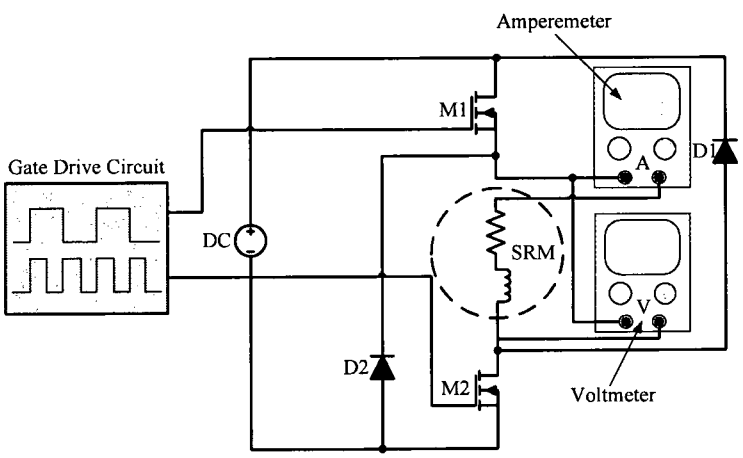

Fig. 3-2 Experimental layout of the direct DC test method

The primary advantage of this method is that the switches (MOSTETs) are controlled by the signal generator, so that the phase current can keep increasing until it reaches its maximum value. Thus, the chances of incorrectly estimating the maximum value of inductance will be diminished significantly. Moreover, as the name of the method suggests, the DC source is used directly, instead of using an intermediate conversion process, from the AC source. Thus, the harmonic issue will be addressed before the experimental results are disturbed.

Nevertheless, the drawbacks of this method are also worth noting. First of all, the saturation problem is not completely solved. When the test is carried out, the tested phase-current needs to be adjusted, to avoid the error in losses; otherwise, the accuracy of the calculated inductance will affect the quality of the SRM model. Secondly, the measurement of phase-voltage and phase-current are accomplished by a voltmeter and ammeter, and hence, the recorded results are root mean square (RMS) values. Based on the relationship between current and inductance for an RL circuit, as shown in (3-1), the phase inductance can be estimated by (3-2) [39].

$$I = \frac{V}{R}(1 - e^{-\frac{R}{L}t}) \tag{3-1}$$

$$L = \frac{1}{2\pi f}\sqrt{(\frac{U_m}{I_m})^2 - (R_p)^2} \tag{3-2}$$

U_m and I_m are the measured phase-voltage and phase-current, respectively, R_p is the phase resistance, and f is the switching frequency. Due to high magnetic saturation of the SRM rotor, the peak as well as minimum value of the measured results needs to be taken care of. For example, the maximum current value could be as much as 5 times that of the corresponding RMS value [41], thereby proves potentially hazardous, and

eventually burning the phase winding. In addition, the estimated results of inductance, from the RMS value of current, cannot be used to accurately represent the relationship between respective instantaneous values. The main reason is that when the instantaneous value of current goes negative, while the switch is off, the RMS value is maintained positive [41].

3.3 PROPOSED CURRENT SATURATION METHOD FOR SRM INDUCTANCE MEASUREMENT

The 2 aforementioned techniques have similar drawbacks, wherein the inherent error for the machine losses are not well considered, while carrying out machine tests. The proposed method will be discussed in this section, and the way of minimize the machine losses is studied in detail.

Apart from the above-discussed techniques, there exist other methods, which are also proposed in literature for SRM inductance measurement. However, their experimental setups are much more complicated and exceedingly specific devices are required. Most SRM inductance measurement techniques involve tremendous cost and time consumption. Thus, this paper proposes a much simpler exclusive current saturation method [42], using an uncomplicated experimental setup to achieve accurate results.

3.3.1 GENERAL IDEA OF THE PROPOSED METHOD

The proposed method primarily makes use of a DC voltage applied to the phase of the SRM winding under test, with its rotor blocked in a fixed position. A suitably sized capacitor is connected in parallel with the DC power source. Instead of using 2 MOSTETs and the gate drive circuitry, the proposed method makes use of a single

MOSFET, connected with an asymmetric function generator. In order to estimate the phase current, a small resistor with high power capacity is employed, connected in series with the tested phase. Moreover, 1 freewheeling diode is also used in parallel with the motor phase and the resistor, so that power can flow while the MOSFET is off. A digital oscilloscope is used to record the phase voltage of the motor and the phase current estimated from the voltage across the added resistor. A computer is used to handle the data obtained from the experiment through a data bus, connected with the oscilloscope. The entire circuit setup for the proposed technique is shown in Fig. 3-3.

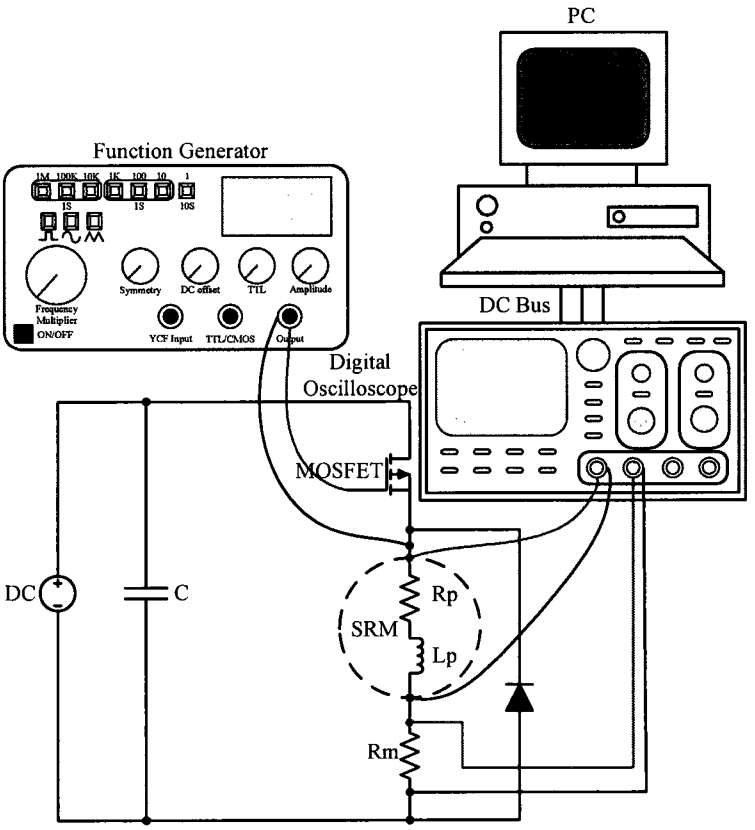

Fig. 3-3 Experimental setup of the proposed current saturation method

The saturation status of the phase inductance can be fully observed by adjusting the symmetry knob, which controls the T_{on} and T_{off} status of the MOSTET. In order to minimize the error introduced by iron losses, 1Hz is chosen to be the working frequency.

Besides, the usage of an appropriately sized capacitor is necessary to ensure that the phase current keeps on increasing till it reaches the saturation region. The function generator working in the asymmetric mode serves 2 purposes: one is to generate the square waveform to trigger the switch; the other is to ensure the off time much longer than the on time, so that the capacitor will be fully charged after releasing all the power from the inductance. Since only the rising part of the current curve needs to be assessed, the classic SRM inverter (two switches per phase topology) is not necessary. While the position changes, the knob of the function generator needs to be readjusted, in order that the peak value of the current reaches the saturation area.

3.3.2 CONSIDERATION OF MACHINE LOSSES

In order to model the magnetic characteristic of an SRM more precisely, the way to minimize the machine losses should be considered. Since the current waveform of an SRM is not sinusoidal, the estimation of copper loss becomes complicated [43], [44]. When an AC voltage is applied, machine losses become hard to distinguish from each other; both of the above mentioned losses exist. While the motor is running at a low speed, the copper loss is dominant; otherwise, the iron losses are dominant. The equivalent circuit of an SRM with AC voltage is shown in Fig. 3-4, where R_{copper} is connected in series with the phase winding.

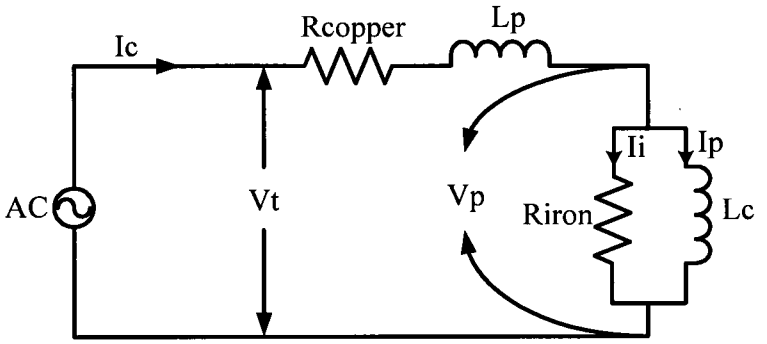

Fig. 3-4 Equivalent circuit of an SRM, with AC supply voltage

I_c is the copper current, I_i is the current flow through the iron, I_p is the phase current, and L_c represents the coupled inductance, which provides the torque to rotate the motor. To be specific, L_p is included as a parasitic inductance. However, since L_p is too small compared to L_c, it can be ignored for the purpose of analysis. Based on Fig. 3-4, it is obvious that the phase current does not equal to the copper current. Moreover, the terminal voltage V_t does not equal to the phase voltage V_p, either.

To estimate the resistive component of the copper losses, a DC current source could be employed, which eliminates the affect of iron losses. Since the current is fixed and the rotor is blocked, the magnetic field cannot change with time. Hence, the phase inductance acts as a short circuit, shorting the resistive component of the iron losses. Hence, Fig. 3-4 can be redrawn as Fig. 3-5, where I_c is equal to I_p, and V_t is equal to V_p. R_{copper} can be estimated simply by using the V_p/I_p relationship.

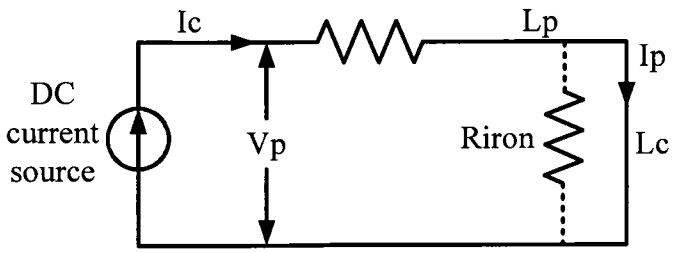

Fig. 3-5 Equivalent circuit of an SRM, with DC supply voltage

The aforementioned DC test method uses a similar arrangement to estimate the resistive component of the copper losses, as a pre-measurement. However, instead of using pure DC, a pulsed DC voltage is applied. As mentioned earlier, since the magnetic field changes due to the AC component included in the DC source, iron losses still exist.

The iron losses or core losses coexist with the copper losses, which consist of eddy current losses as well as hysteresis losses. According to [45], the eddy current losses are proportional to the square of the flux density and the frequency.

$$P_e \propto K_e \cdot B^2 \cdot f^2 \tag{3-3}$$

Here P_e is the power loss due to the eddy current, B is flux density, f is the frequency, which reflects the operating speed, and K_e is a constant parameter. The eddy current losses can be minimized by improving the original design, such as lamination, using highly resistive or low conductive material, and reducing the size of the martial (or increasing the cross sectional area of the material.

It is complicated to separate hysteresis losses from eddy current losses, because they are determined by the same components. Referring to [45], the hysteresis losses are proportional to the product of the maximum value of flux density and frequency.

$$P_h \propto K_h \cdot B_{\max} \cdot f \tag{3-4}$$

Here, P_h represents hysteresis losses and K_h is a constant parameter. To simplify the scheme of the model with respect to iron losses, a resistor R_{iron} is connected in parallel with the phase winding, as depicted previously in Fig. 3-4. Since the machine is fixed, the material could not be changed; the only way to minimize the iron losses is to decrease the frequency and the applied DC voltage.

The proposed method applies low voltage and low frequency to minimize the iron losses during the measurement. Since the operating frequency is low, the copper loss will be dominant. The copper loss resistor is estimated during pre-measurement. Hence, the resistive voltage drop introduced by the copper resistor is eliminated. In addition, since the T_{on} time is much shorter than T_{off}, the phase winding will not heat up and affect the experimental results.

3.4 EXPERIMENTAL RESULTS AND ANALYSIS

This section will present the experimental results, including the operating principle, especially the processing of numerical data. Eventually, the experimental based magnetic characteristics will be compared with the results obtained by Finite Element Analysis.

3.4.1 EXPERIMENTAL RESULTS USING CURRENT SATURATION METHOD

The proposed current saturation method uses a 24V, 3.2A DC voltage source and a 0.25Ω external resistor. The asymmetric function generator works at 1Hz, and T_{on}/T_{off}= 1/10. The motor under test is an OULTON 8/6 SRM, with a rated power of 7.5kW, shown in Fig 3-6 [46]. Since one electric period is 60°, the experimental measurements are started from the rotor at 0° and ended when the rotor is at 60°. At each rotor position, the voltage across the phase of the SRM and the external resistor are recorded, using a digital oscilloscope, with a sampling time at 10ks/s. Through a computer, the value of the voltage across the resistor is routinely converted into current, for further calculations.

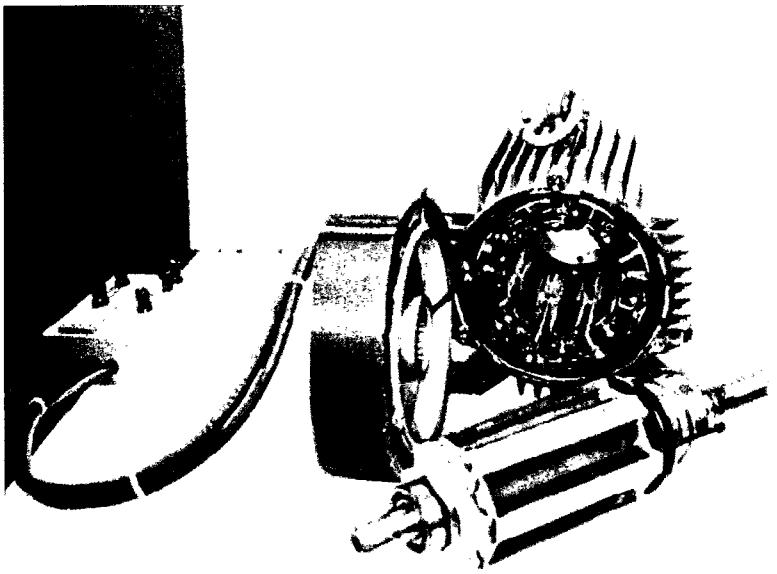

Fig. 3-6 OULTON 8/6, 7.5kW, 4-phase SRM [TASC Drives Ltd., UK]

However, while carrying out the experiment, the obtained results are affected by two types of noise, namely electronic noise and quantization noise. The former is inherent in all electronic devices. Depending on the circuit, electronic noise can be amplified greatly. Quantization noise is a kind of quantization error introduced by the analog to digital conversion (ADC), inside the digital oscilloscope. The screen of the oscilloscope presents the round-off error between the analog input and the converted digitized output. Hence, an appropriate filter is necessary; a numerical dynamic filter has been presented, to filter each output result from the oscilloscope. The obtained waveform from the oscilloscope, before adjustment, is shown in Fig. 3-7.

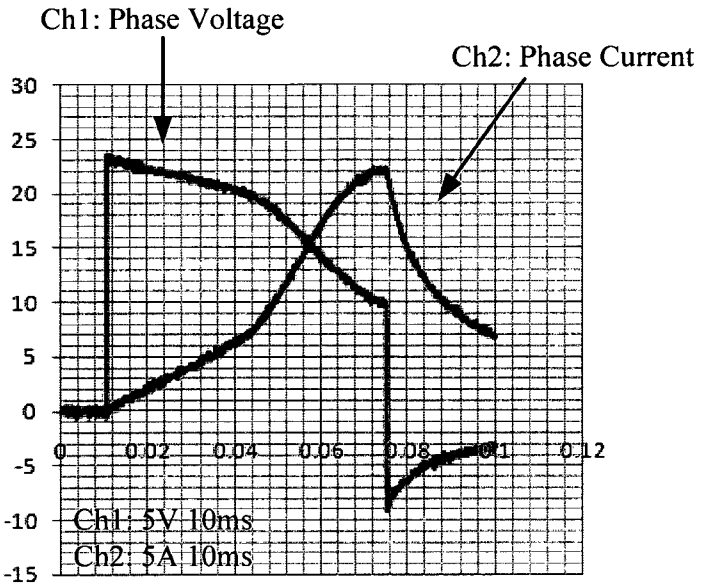

Fig. 3-7 Measured phase voltage and current waveforms

Since both the voltage and current will be used for future calculations, the previous adjustment is necessary. To reduce the noise included in both curves, a moving trapezoidal weighted numerical filter is designed as follows:

$$Y(t)=\frac{\sum_{n=-j}^{0}\frac{1-2n}{10}X(t_n)+\sum_{n=0}^{j}\frac{2n+1}{10}X(t_n)}{2\cdot\sum_{n=0}^{j}\frac{2n+1}{10}},j=1,2,3,4 \tag{3-5}$$

The numerical filter yields the weighted data multiplied with the former data and latter data, around the awaiting processing data. It is worth noting here that the number of former as well as latter data should be equal. After the summation, the total weighted value of the processed signal will be divided. Since the reference data changes along with the processed data, the filter is actually moving with the curve measured by the oscilloscope. The range selection of the reference data should be sufficiently large to avoid high frequency noise. In the proposed method, 10 reference data are used for filtering. The results of the filtered measurement data are shown in Fig. 3-8, which

presents the curves smoothened by the filter; the magnitude and shape remaining unchanged. Furthermore, Fig. 3-9 shows the FFT version of the original signal with filter and the filtered results.

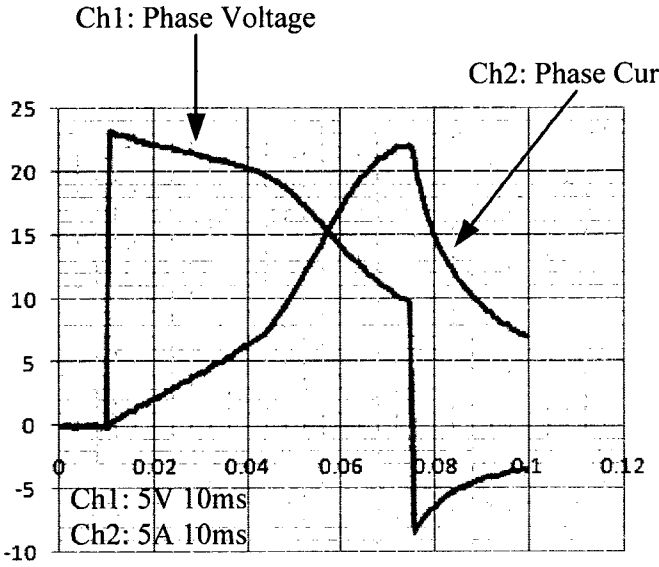

Fig. 3-8 Filtered experimental results

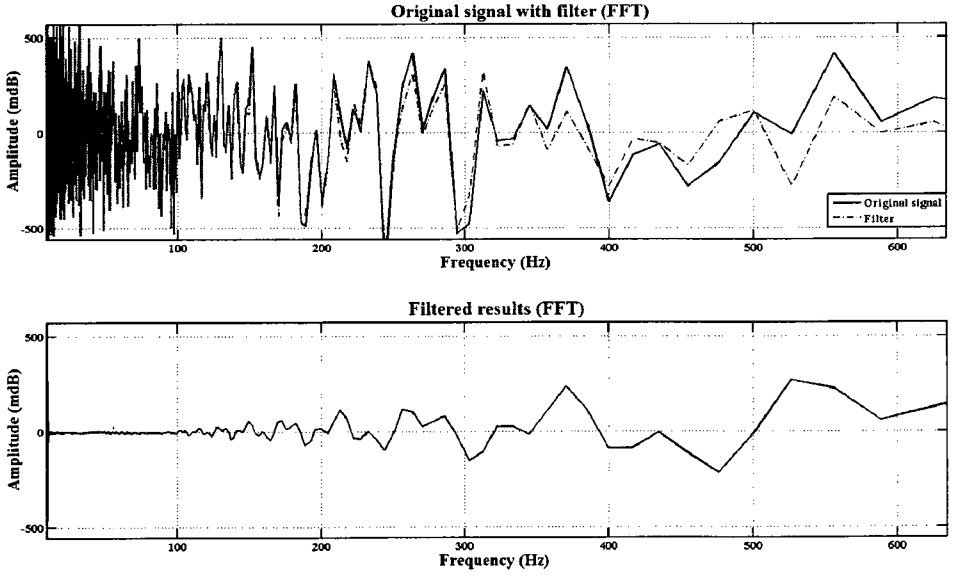

Fig. 3-9 The FFT of the original signal and the filtered results

As and when measurement results are recorded by the digital oscilloscope in one position, the data automatically gets transferred to the computer for analysis, and then the same procedure is repeated till all rotor positions in one electric period are measured and recorded. The proposed method keeps increasing the phase current until the saturation region is reached, for each rotor position. Neglecting mutual inductance between phases, the applied phase voltage can be expressed by

$$V_{ph} = RI_{ph} + \frac{d\lambda(\theta, I_{ph})}{dt} \tag{3-6}$$

Here, V_{ph} is the phase voltage, R is the phase resistance, I_{ph} is the phase current, λ is the flux linkage and θ is the rotor position. The flux linkage and inductance are a function of rotor position and current and their nonlinear relationship can be referred to (2-1) in previous chapter.

As equation (3-6) indicates, phase voltage comprises of three parts: resistive voltage, inductive voltage, and induced EMF (back-EMF). The rotational speed does not directly affect the inductance value. However, speed does affect phase voltage, and also, based on the definition of "energy stored in an inductor;" it will directly affect torque production. During the saturation period, the current curve is almost flat, and the inductive voltage goes to zero, due to fixed current. Besides, because the rotor is fixed, the rotor position cannot be changed. Thus, the back-EMF part will be eliminated. Hence, according to (2-1), phase voltage will only depend on phase resistance.

It is interesting to note that the estimated phase resistance is not equal to the pre-measured copper resistance. In fact, a small component resistance appears during the inductance profile measurement. Since the voltage applied on the phase terminal is a DC voltage, with an AC component, the iron losses still exist. To model the SRM magnetic

characteristics precisely, a small resistance should be considered as well, called R_{loss}. The phase resistance can be expressed as a combination of copper resistance and R_{loss}. For different rotor positions, the value of R_{loss} is slightly different, due to varying flux densities. During the T_{on} period, the phase current keeps increasing, the resistive voltage drop increases, while the inductive voltage decreases, until it becomes zero. The details are depicted in Fig. 3-10, where the shaded portion is the varied resistive voltage, contributed by R_{copper} and R_{loss}.

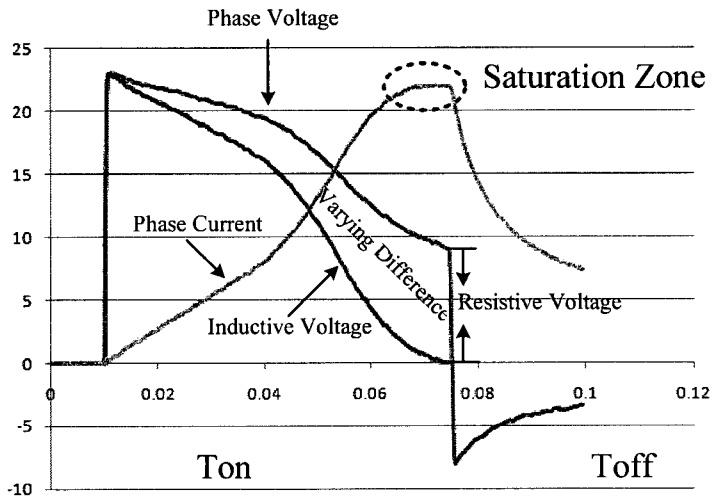

Fig. 3-10 Relationship between resistive voltage and inductive voltage

The flux curve is obtained using (2-2), and the resistive voltage drop in the calculated resistor, during the experiment, is subtracted. The pre-measured copper resistance could be considered dominant over the phase resistance. Figs. 3-11 and 3-12 present the magnetization characteristics of the SRM and phase inductance for the entire electric period, respectively. The 3-D version of the inductance profile is shown in Fig. 3-13, which presents the model of the SRM more precisely.

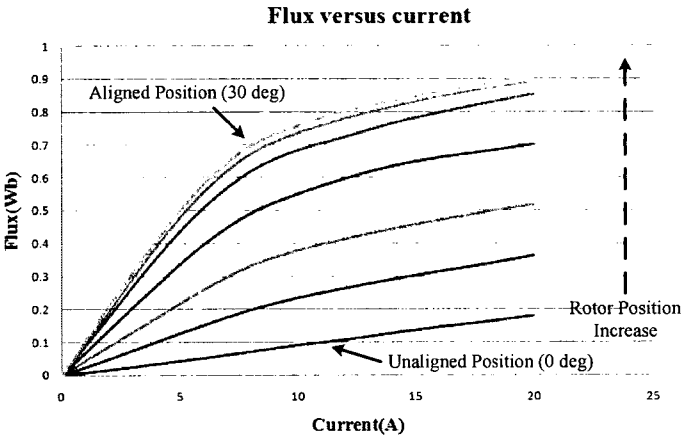

Fig. 3-11 Magnetization characteristics of the SRM, based on experiments

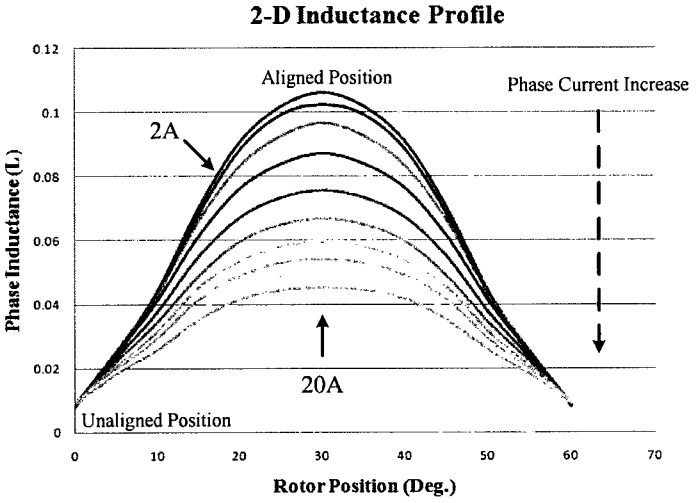

Fig. 3-12 2-D phase inductance profile, based on experiments

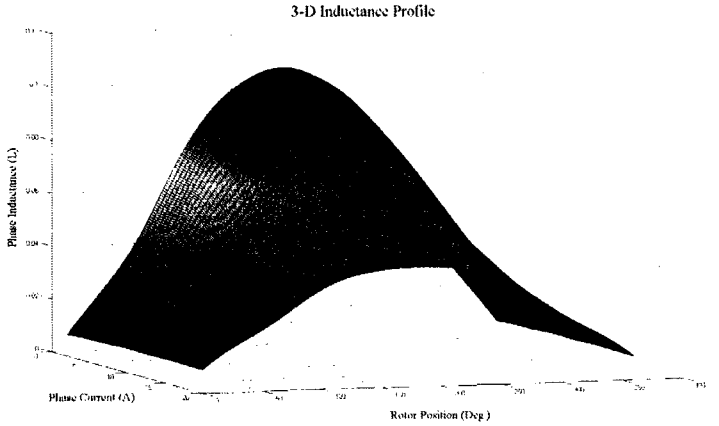

Fig. 3-13 3-D plot of the inductance profile

As is clear from the above plots, the flux curves are close to each other, while approaching the aligned position, the reason being that manufacturers are usually willing to couple fluxes at high saturation positions, in order to improve torque production. The measured position starts from the unaligned position (0°), 5°, 10°, 15°, 20°, 25°, and ends at the aligned position (30°). The measured current is from 2A to 20A, for each rotor position. The variation tendency is presented in the previous figures. Moreover, the 3-D inductance profile clearly depicts the dependency of phase inductance on rotor position and phase current.

3.4.2 FINITE ELEMENT ANALYSIS (FEA)

The Finite Element Method was used to approximately build a numerical model of the system. The FEA model of the experimental motor was built using the FEMM software. Table 3-1 summarizes the geometric parameters from the manufacturer [46], and the tested SRM flux model is shown in Fig. 3-14.

Table 3-1 Geometric information of the 7.5kW OULTON SRM

Geometric Parameter	
Number of rotor poles	6
Number of stator poles	8
Stator outer diameter	204mm
shaft diameter	36.6mm
Stator pole arc	20.1°
Rotor pole arc	23.6°
Air-gap length	0.6mm
Turns per pole	70

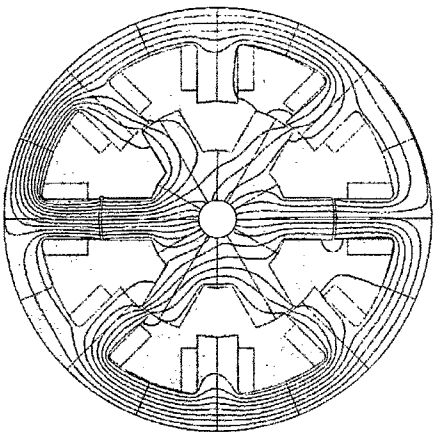

Fig. 3-14 FEA based flux model of the experimental SRM

The FEA simulation is only used as a reference framework, for accuracy verification for the aforementioned techniques. Details of the FEA method are not presented here; however, the comparative aspects of the analysis are discussed. The flux curve obtained by FEA is compared with that obtained from experimental results, as shown in Fig. 3-15.

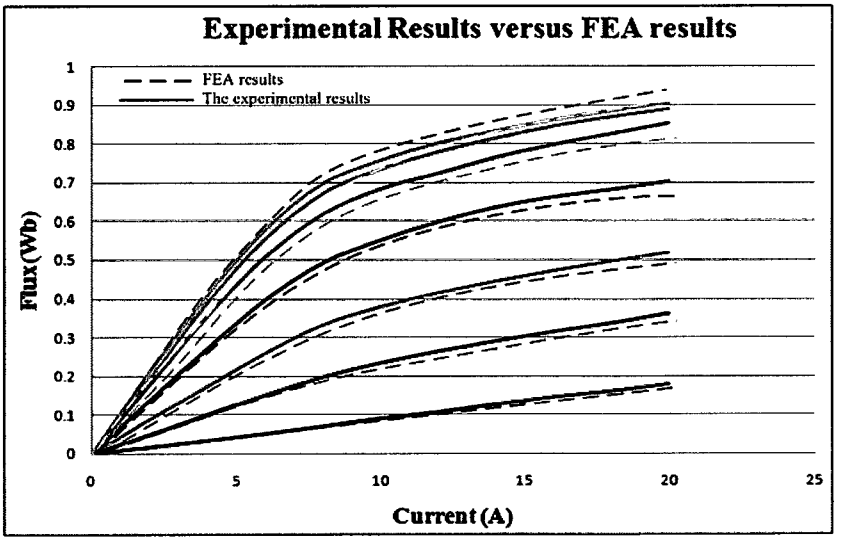

Fig. 3-15 Comparison between experimental and FEA results

In general, the FEA results are widely acceptable, due to the difficulty of modeling the non-linear SRM characteristics. However, the FEA based flux curves

predict higher values than those of the experimental results, especially in the aligned position; the FEA based flux curves present much stronger saturation ability than the measured curves. The major reason for this difference is the error during modeling of the iron magnetization curve (B-H curve). Moreover, the software assumes that the material for the iron is 3.25% SiFe, with a saturation density of 1.7T [47]-[49], because the material data is the protected property of the manufacturer.

The FEA computations for both unaligned and aligned positions are the first stage during analyzing the model. Since the aligned position easily approaches the saturation region, the iron manufactured by using high magnetization material, saturates more easily. Furthermore, few errors could occur due to the issue related to the real value of the air gap. Due to the complication of the processing technique, the real value of the air gap could be different than the value indicated on the datasheet. Even a small difference in the value of the air gap will yield a significant difference between the measured value and the FEA based results [50]. The estimated phase resistance error might be another reason for the minor variation between the experimental and FEA results.

3.4.3 Comparison Between Proposed and Conventional Methods

The experimental results obtained by the proposed current saturation method and the previously mentioned conventional methods are shown in table 3-2.

Table 3-2 Comparison of inductance values at unaligned and aligned positions

Inductance Values for Different Current at Unaligned Position (H)				
Current	AC/DC Test	Direct DC Test	Proposed Current Saturation	FEA
4	0.008503	0.008612	0.008482	0.0085
8	0.008876	0.00899	0.008838	0.0087
12	0.009027	0.009167	0.008874	0.0088
16	0.009247	0.009496	0.009102	0.009
Inductance Values for Different Current at Aligned Position (H)				
Current	AC/DC Test	Direct DC Test	Proposed Current Saturation	FEA
4	0.098738	0.096434	0.102304	0.1031
8	0.092314	0.081325	0.088178	0.0906
12	0.07486	0.058719	0.066834	0.0685
16	0.061385	0.04412	0.053851	0.0557

In this table, the inductance value for the low current and high current are presented at the unaligned position and the aligned position separately. Meanwhile, the FEA based simulation results are added in the table as a frame of reference, to verify the accuracy of each method. According to the table, the experimental results of the proposed method are much closer to the FEA reference values. It is evident that the proposed current saturation method is more accurate than the others. The DC test has the issue of measuring root-mean-square (RMS) values, which are discussed in section 3.2, whereas the AC/DC test provides acceptable results in the low current region. It is worthwhile mentioning here that magnetic saturation of the stator is not yet present. Hence, applying the current saturation method is a straightforward and accurate method to obtain the inductance profile.

3.5 SUMMARY

This chapter reviewed two popular conventional methods for SRM inductance measurement. However, both methods seriously suffer from ambiguity due to machine losses. Hence, a novel, more efficient current saturation method is introduced, to model the SRM inductance profile. The novel technique uses low frequency and low voltage to minimize the influence of iron losses. Compared to classic methods, the proposed method is capable of higher accuracy, as was evident from the experimental. Moreover, the experimental setup of the proposed novel method is also uncomplicated. However, the switch ratings should be taken care of, due to sudden current rise during triggering. Furthermore, any loose contact between the components inside the circuit will destroy the switch. A suitable isolator can be used to protect the oscilloscope, if required.

During the experiment, two types of noise were noticed, namely electronic noise and quantization noise. To tackle this practical issue, this chapter also proposed a specially designed moving trapezoidal weighted numerical filter. The filter yields the weighted data multiplied with the former data and latter data, around the awaiting processing data. Besides, the range selection of the reference data is sufficiently large, to avoid high frequency noise, in order to obtain expected and accurate results.

It was understood that the differences between the measured and FEA results are due to unknown material characteristics. The tested SRM is a commercial product, and hence, manufacturers have obviously not published material details. The inaccurate air gap value could be considered as another error. The proposed technique represents a new tool to approach a true inductive model of the SRM. It is obvious that sensor-less control and off-line control highly rely on accurate inductive SRM models [51], [52]. Therefore,

accurate modeling of SRMs plays a vital role in forming a solid basis for advanced control strategy development.

CHAPTER 4

VOLTAGE-PROFILE TECHNIQUE FOR SRM TORQUE RIPPLE MINIMIZATION

4.1 INTRODUCTION

Based on the knowledge of the previous torque ripple minimization techniques, the common aspect for each methodology is either related to motor design or improved current profile techniques, with turn on/off angle and hysteresis control. In general, the classic techniques focus on the control of operational parameters, which aim at minimizing torque ripple by choosing a suitable phase current, turn-on angle, turn-off angle, and shaft load. In addition, fuzzy logic, neural network, or other iterative techniques have been employed in the past, to deal with the non-linearity. However, the resultant torque ripple is high at high speeds, due to the barely compensated high back-EMF. Even the firing angle strategy is no longer able to handle torque ripples. This chapter introduces a new voltage-profile based algorithm, which targets torque ripple minimization over the entire speed range, thus making it suitable for automotive propulsion applications.

Based on the conventional control strategies, presented in chapter 2, the SRM is controlled through feedback rotor position and applied current. Thus, two control loops are demanded, to adjust the difference between the reference value and the error signal. Along with the increase of speed, the delay between the feedback information and the reference signal increases dramatically. This is essentially true due to the dual control

loops. Besides, there exists the limitation that DC bus voltage is not able to de-energize the phase winding, in order to return flux to zero, before ensuing phase excitation. Keeping these drawbacks in mind, this chapter suggests a scheme that uses information of the phase voltage instead. The developed voltage-profile algorithm uses an off-line calculation technique, before performing control operation. This is most likely the best approach to omit the current loop. Moreover, such a strategy also eliminates the voltage limitation, due to the adopted pre-regulation procedure. A finite approximation approach (Newton method) is applied to compute the possible voltage-profile, using an iterative calculation. Moreover, the obtained inductance model though an experimental setup causes the resultant voltage-profile to be exceedingly practical and accurate. Finally, the obtained voltage-profiles over the entire speed range are stored in a look-up table, with indices as speed and rotor position for future control purposes.

In addition to the control methodology, this chapter also introduces the main parameters that affect the voltage-profile calculation. By increasing or decreasing the value of these critical parameters, the shape of the voltage profile can be changed, and concurrently, the resultant torque ripple can be varied. The range of variation of the different parameters over the entire speed range is summarized, in order to simplify the program, and reduce time and memory required for calculation. Memory expenditure is an important consideration, due to the immense look-up table information. A calculated PWM cycle for different speed ranges is preferable, before importing the entire data into the memory. It is clear that some data is repeated, based on specific rotor positions. Furthermore, it is not necessary to generate PWM frame-by-frame. In fact, the high frequency of PWM generation could introduce redundant semiconductor losses within the

motor drive. In order to optimize the PWM cycle for each speed range, the look-up table includes the PWM cycle information, which also minimizes memory usage.

4.2 VOLTAGE-PROFILE ALGORITHM

In order to avoid the issue related to current regulation, using the proposed technique, the current feedback loop is eliminated, which improves the response rate of the controller. Moreover, a programmed off-line controller is proposed in this section, instead of employing a real-time implementation controller. This section is separated into two parts; part one focuses on the finite approximate approach (Newton method), while part two describes the torque ripple minimization technique in detail.

4.2.1 FINITE APPROXIMATION APPROACH (NEWTON METHOD)

Due to the highly non-linear nature of the SRM, calculation for the desired voltage value, with the aim of torque ripple minimization, is fairly complicated. According to the SRM principle of operation, discussed in chapter 2, the voltage is determined by the applied current, the angular velocity, and the rotor position. All three parameters vary simultaneously and are highly interrelated. In order to address this issue, the finite approximation approach (Newton method) based iterative calculation is utilized. The finite approximation approach facilitates the calculation of corresponding current, while keeping the voltage value fixed, for a certain rotor position. Based on the equation 2-1, it is clear that current cannot be determined by any assumed voltage, due to the non-linear complexity. Hence, it is desirable that the approximation be nearly equal to the expected voltage.

In order to better understand the finite approximate technique, consider the following explanation: suppose equation (2-1) is $f(x)$, the assumed voltage is yielded result y, and the value of applied current is considered as x_n, where n varies between zero and the pre-defined value. The important point to consider here is the position where the curve passes the x-axis geometrically [53]. The finite approximate approach always starts with an assumed value, x_0, which is inserted into the curve, yielding $f(x_0)$. Thereafter, a tangent is drawn through the $f(x_0)$ point, which intersects the x-axis, whereby y_0 is yielded using the function 4-1:

$$y_0 = f(x_0) + f'(x_0)(x - x_0) \tag{4-1}$$

Here, x_1 is the intercept of the $f(x_0)$ tangent line and the x-axis, which can be calculated by the following function:

$$x_1 = x_0 - \frac{f(x_0)}{f'(x_0)} \tag{4-2}$$

The next step is to obtain an improved estimate solution, by replacing the initial guess, x_0, with x_1. Repeat this procedure by changing x_1 with x_2 using equation 4-3:

$$x_2 = x_1 - \frac{f(x_1)}{f'(x_1)} \tag{4-3}$$

The entire procedure is depicted in Fig 4-1. According to the described procedure, the first estimation, x_1, is close to the true root, compared to the initial guess, x_0. Thereafter, the following estimated value, x_2, is closer to x_1.

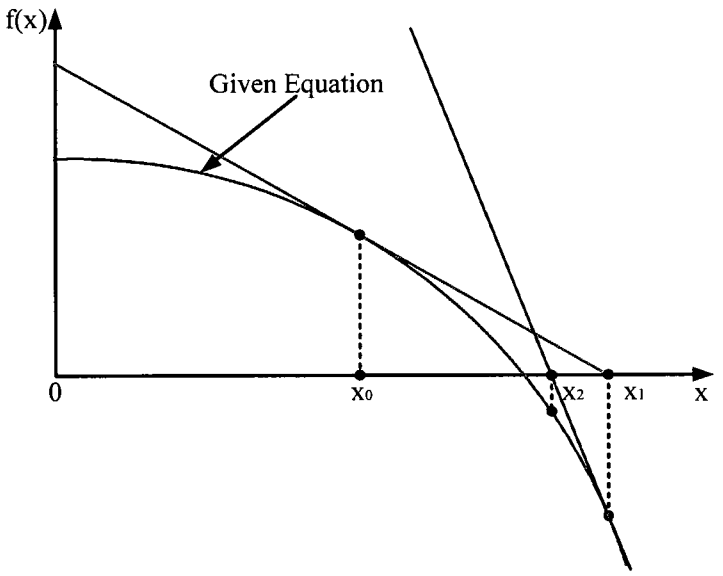

Fig. 4-1 Graphical representation of the finite approximation approach (Newton method)

Numerous of intercept points are generated, in addition to the iterative calculation. Finally, x_n is calculated using equation (4-4), and the tangent line is obtained using equation 4-5 [53], [54].

$$x = x_n - \frac{f(x_n)}{f'(x_n)} \tag{4-4}$$

$$y = f(x_n) + f'(x_n)(x - x_n) \tag{4-5}$$

The finite approximate approach (Newton method) is summarized in equation 4-6 [53], [54], where n is a pre-defined number, which indicates the iterative loop-cycle index.

$$x_{n+1} = x_n - \frac{f(x_n)}{f'(x_n)} \tag{4-6}$$

Since the estimated value is infinitesimally close to the true root, the accurate ratio needs to be defined before executing the program. In order to avoid formation of an endless loop, the masks triggered by the condition statement need to be configured inside each iterative cycle. If the desired value cannot be obtained, the initially assumed data or the

accurate ratio needs to be redefined. Once the estimated current corresponding to the predefined voltage profile is obtained, the iterative calculation for the ensuing rotor position is activated. Finally, the complete current profile is estimated over a particular speed range.

4.2.2 Voltage-Profile Calculation for Torque Ripple Minimization

In order to achieve the goal of torque ripple minimization, an appropriate voltage-profile for each speed range needs to be obtained. This calculation is based on a sophisticated iterative program, coupled with data analysis techniques [55]. For the purpose of high accuracy, the program runs for each selected speed range, which is separated by the step of 100 rpm. The entire program can be simply divided into two parts: the preparation part and the iterative calculation part.

For the first part, speed information is required. Once speed value is obtained, the program automatically searches for an initial voltage profile. In this case, the parameter calculation is implemented in the background processor; details will be discussed in the ensuing section. Thereafter, the rotation speed (rpm) will be converted to electrical angular velocity, for execution of the next step. The value of $dL/d\theta$ is calculated for different currents, for all rotor positions, and a 3-D look-up table is generated for the supplementary utilization. Thereafter, the initial current value for each speed range is set, and a dedicated table for those current values, corresponding to specific speed values, is established, for further reference. Before running the iterative program, an initial current value is selected from the data, in order to start the finite approximate approach.

The second part of the program is directly dependant on the previous part, wherein the initial current is first chosen. The corresponding current-profile is subsequently calculated, based on the initial voltage-profile, which is formed before the iterative program. Next, the phase torque and total torque can be calculated, based on the obtained current data. Hence, the torque ripple can be accurately estimated for the selected voltage-profile. In addition, the mean square error (MSE) of the torque ripple is used to produce a more accurate estimate, in order to evaluate the quality of the resultant torque. If the torque ripple is acceptable, the voltage-profile will be stored, and the data will be saved into the look-up table, with index of rotor position and speed. Otherwise, the obtained voltage profile will be added or subtracted ($\pm\Delta V$), and the iterative part will run again. Fig. 4-2 shows the flow chart of the complete program.

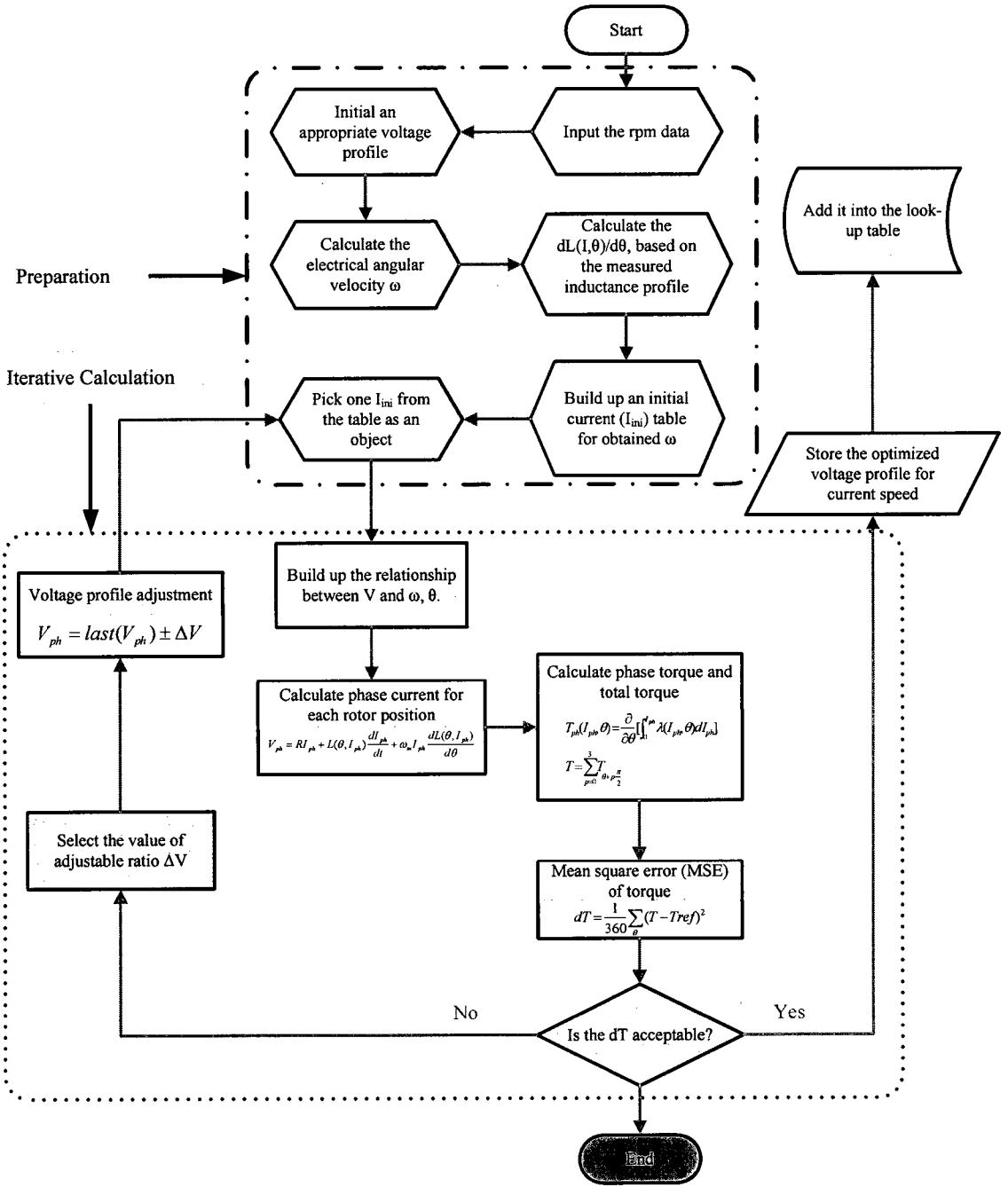

Fig. 4-2 Finite approximation based voltage profile algorithm

To ensure that the program runs effortlessly, limiters and protectors (masks) need to be configured in the iterative part of the program. Due to the mechanical and electrical characteristics of the target SRM, the speed cannot beyond 8000 rpm and the current is limited to 20A. The protector will be triggered if the collected data is over the limit. In

addition, the expected difference ratio between the estimated current and the real current should be checked before starting the program. More specifically, the difference ratio can be zoomed in or out in a certain range (1~3%), based on the rotational speed. Too many iterative cycles may consume additional time. However, only a small amount of the loop may result in a bad estimation. Hence, the numbers of loops and accurate ratio have to be adjusted, before carrying out the program.

4.3 CALCULATION OF PARAMETERS FOR VOLTAGE-PROFILE INITIALIZATION

The program begins its iteration using an initial voltage-profile, followed by few numerical solving techniques. Thus, the resultant torque ripple will be obtained. In the case of iteration, a simple derivative based approximation is used, and the new voltage-profile is produced. Once the expected torque ripple is obtained, the corresponding voltage-profile is saved with the specified speed. Thus, it is clear that knowledge of the initial voltage-profile is critical to obtain torque. Since the relative torque ripple is minimized before executing the program, the time spent is minimized and overall program complexity is reduced. Therefore, a pre-calculated initial voltage-profile, at different speeds, is preferable. The resultant torque ripple, based on the crude voltage as well as calculated voltage, is summarized in Fig. 4-3.

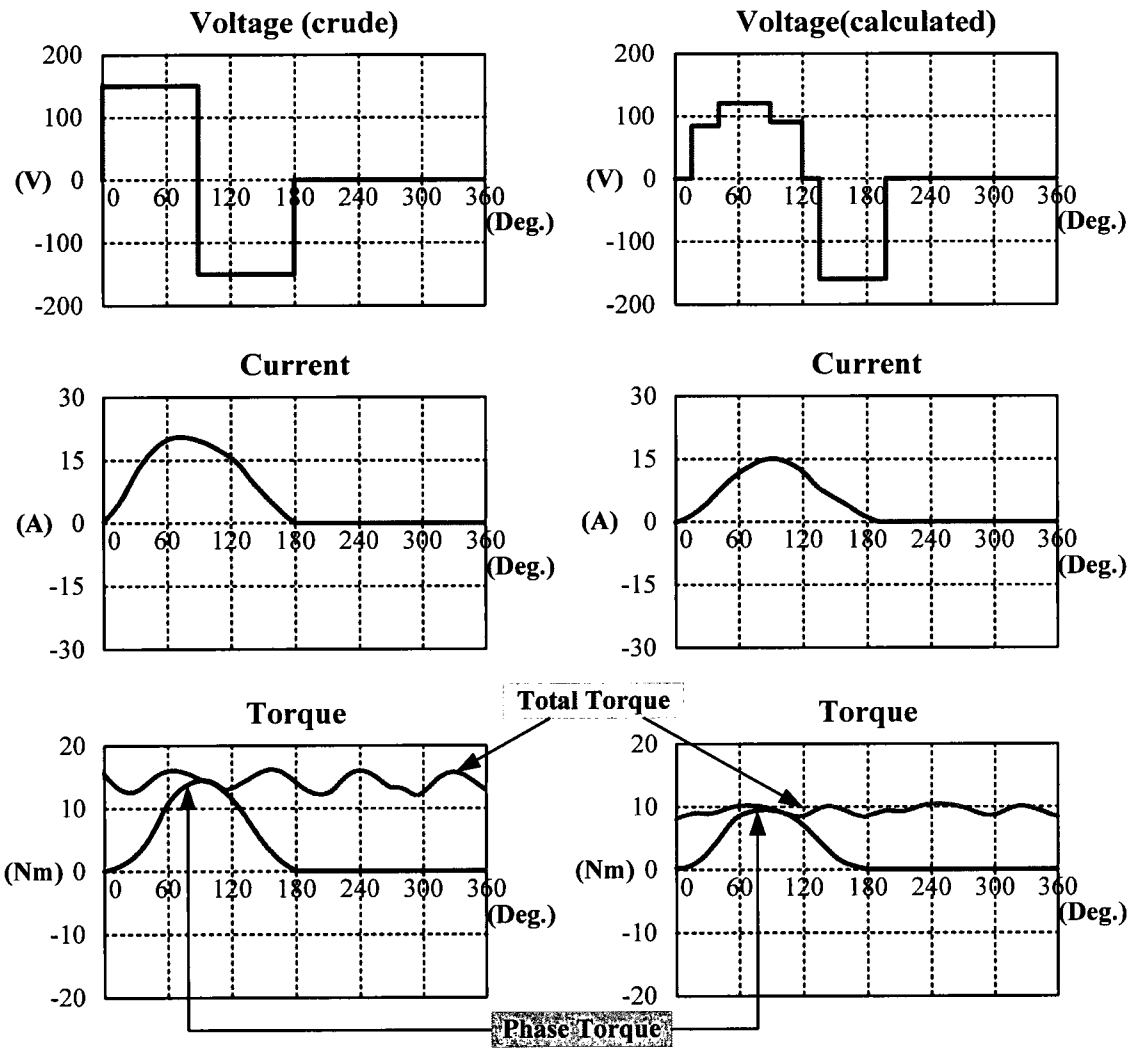

Fig. 4-3 Torque ripple affected by different voltage-profiles

Fig. 4-3 presents the different voltages applied across the SRM. Subsequently, the phase current is estimated and torque is yielded. It is clearly observed that the calculated voltage-profile results in a lower torque ripple, compared to the unprocessed voltage-profile. Therefore, in order to save a fair amount of machine time, it is meaningful to calculate the operating voltage, before carrying out the iterative program. After a series of attempts, the critical parametric boundaries were identified, which directly impact the resultant torque ripple shape. The critical parametric boundaries that affect the torque ripple are highlighted in Fig. 4-4.

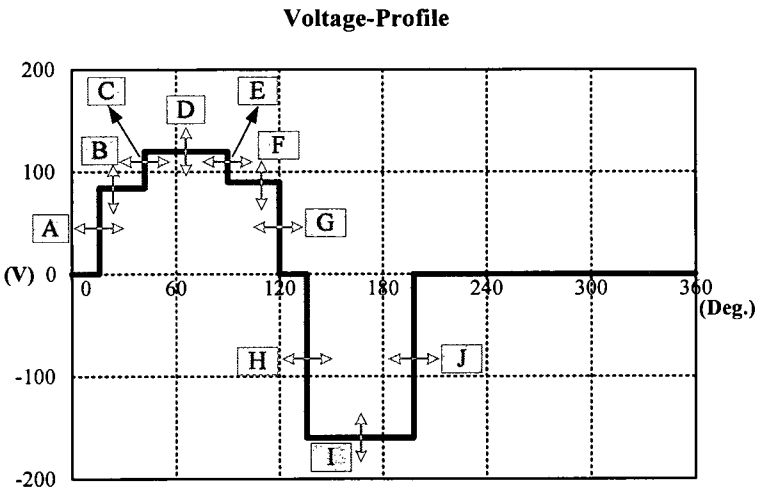

Fig. 4-4 Critical parameters for voltage-profile initialization

As shown in Fig. 4-4, the parameters are cataloged into the lateral variations and longitudinal variations, where *A*, *C*, *E*, *G*, *H*, and *J* belong to lateral variations, and *B*, *D*, *F*, and *I* belong to longitudinal variations. During the off-line control (program execution) period, *A* and *G* represent the turn on and turn off angles, respectively. *C* and *E* control the range of three longitudinal variations *B*, *D*, and *F*. Also, *H* and *J* control the range of voltage de-energization. At some unique speed, *G* and *H* may overlap each other. However, *H* can never lead *G* in the voltage-profile, due to the SRM operating principle. From the point of view of longitudinal variations, *B*, *D*, and *F* handle the level of produced torque ripple. The parameter, *I*, is used to determine the maximum negative voltage, in order to allow the flux to precisely return to zero, before next power injection. All the parameters may change during different operating speeds. Table 4-1 summarizes the optimized position for lateral variations.

Table 4-1 Lateral variations in voltage-profile distribution

Parameter Position (Degrees)						
Speed (RPM)	A	C	E	G	H	J
500	16	35	87	125	132	195
1000	18	39	87	127	136	195
2000	20	40	89	130	138	197
3000	20	47	90	135	140	199
4000	20	49	93	137	140	200
5000	21	50	97	131	142	201
6000	21	52	101	138	141	200
7000	23	56	108	139	140	201
8000	23	59	112	140	141	205

Meanwhile, *B*, *D*, and *F* represent the amplitude of voltage for different rotor positions. These parameters are recorded after numerous attempted calculations. The parameter, *I*, is always changing, and is accompanied with the value of maximum positive voltage. Furthermore, in order to ensure complete de-energization, the absolute value of *I* is always larger than the maximum positive voltage. The torque ripple influenced by *B*, *D*, and *F* are summarized in Fig. 4-5.

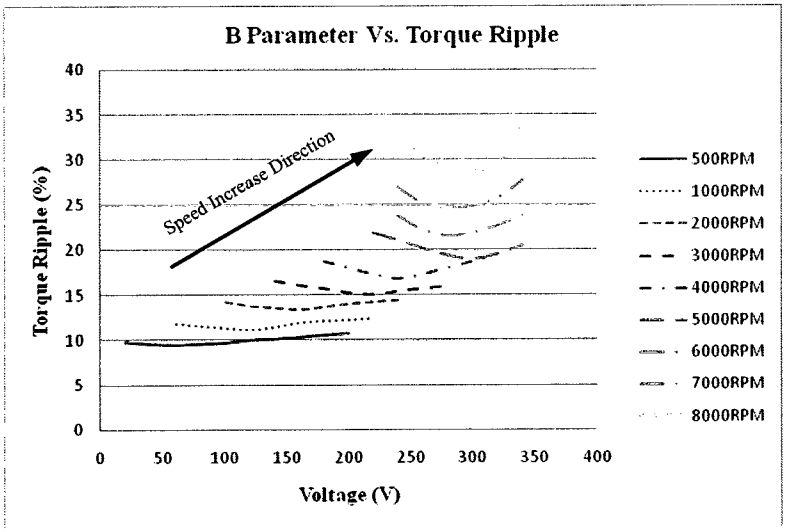

(a) Torque ripple affected by B parameter

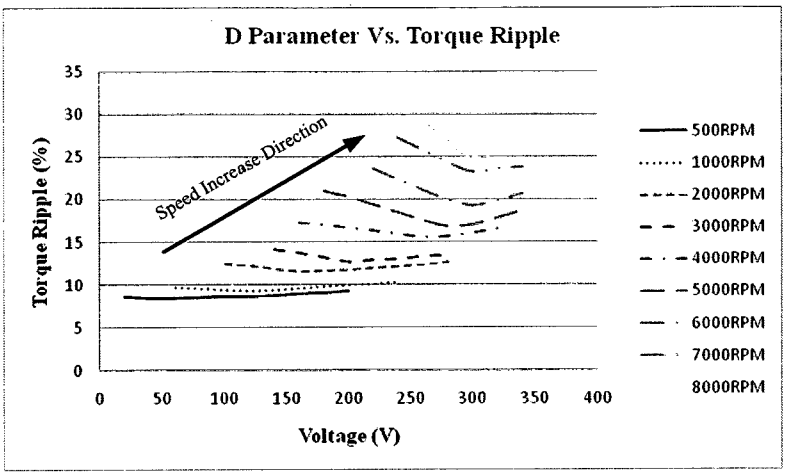

(b) Torque ripple affected by D parameter

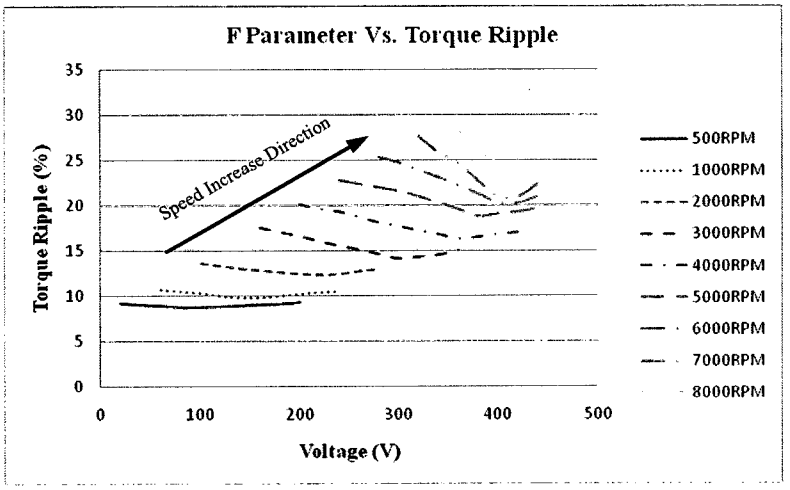

(c) Torque ripple affected by F parameter

Fig. 4-5 Torque ripple affected by parameters *B*, *D*, and *F*

As is clear, all parameters introduce significant torque ripple change at high speeds. In addition, the amplitude of voltage for each parameter tends to converge, while speed increases. However, since all tendencies of torque ripples are recorded, when one parameter acts at each speed, the resultant torque ripple is only considered as a reference for supplementary processing. It is complicated to record the interaction among all the parameters, due to the irregularity of torque ripple verification. Hence, it is preferable to

draw up a scenario for the upper limit of torque ripple, before implementing the iterative program in each speed range.

A change in the parameter, I, does not cause any distinct improvement in torque ripple. However, an inappropriate value for I may yield an erroneous torque value, or even no torque. Thus, the value of I is always set inversely proportional to the maximum value of positive voltage, during voltage-profile initialization. In other words, I is highly dependent on the other longitudinal variations, and its exact amplitude will be found in supplementary iterative calculations.

4.4 PWM Cycle Distribution and Memory Consumption

The voltage-profile algorithm program is complied as m-code, in Matlab, and the calculated data are automatically saved in format, which has 15 significant digits. Thereafter, the optimized voltage-profile for each speed is stored in a look-up table, after the iterative calculation. To reduce memory space occupied by each set of data, only 2 digits after the decimal points are retained. Therefore, the average digit length of voltage data for each speed becomes 4. Hence, each set of data occupies 4 bytes of memory space. However, in order to store all voltage-profile data over the entire speed range (0~8000rpm), approximately 11 MB of memory space is additionally required, which is a hindrance, considering the limited space of on-board FPGA random access memory (RAM).

It must be highlighted, though, that several options do exist, in order to reduce the amount of required memory. Instead of saving the data at each angle, only one data set is used to represent all the data in a PWM cycle. Thus, this data set represents more than one angle. Due to the fact that this in turn reflects a somewhat inferior voltage-profile,

slightly less accurate torque ripples may be introduced at some rotor positions. Thus, a well calculated PWM cycle is extremely essential, for the purpose of data distribution. Furthermore, only one digit is needed for certain positions, due to data information repetition. For example, as discussed in the previous section, the parameter, *I*, and the last position filled with zero, can be replaced by merely one data set. Fig. 4-6 presents the PWM cycle distribution at low speed and high speed.

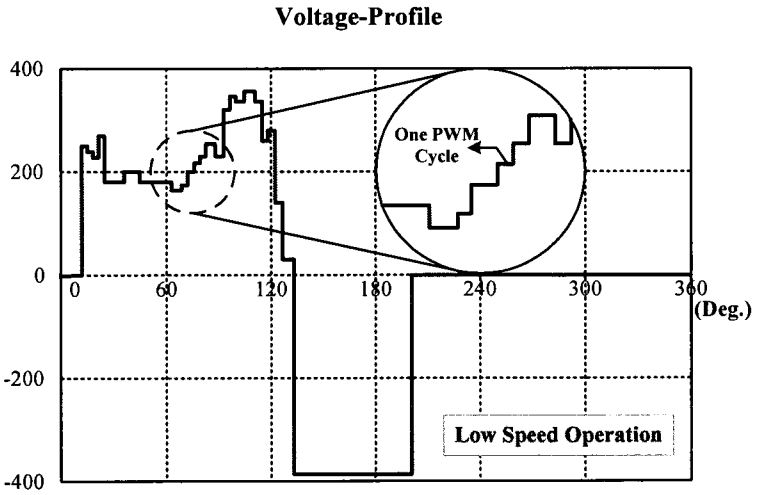

(a) PWM cycle distribution at low speed

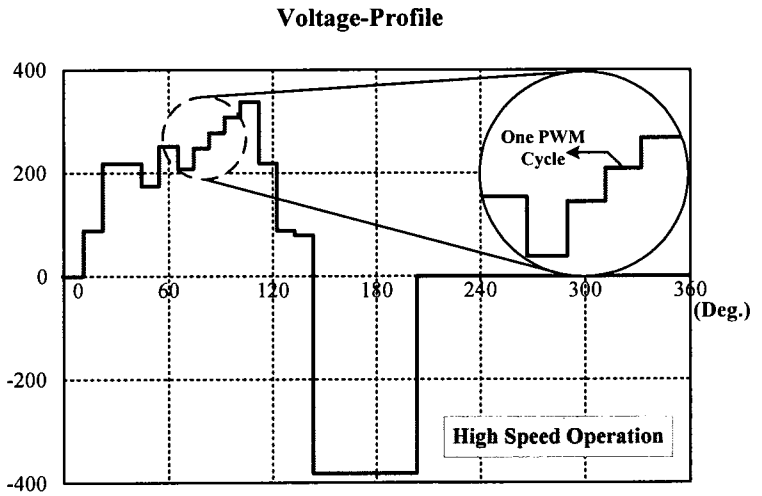

(b) PWM cycle distribution at high speed

Fig. 4-6 PWM cycle distribution over voltage-profile

In order to eliminate the audible component of switching frequency, the semiconductors are demanded to drive the target SRM between 18 kHz to 25 kHz. If the PWM cycle is distributed intelligently, the position information, characterized by repeating information, is represented by only one data set. Thus, more than half of amount of occupied memory space will be released. Table 4-2 describes the memory usage in the SRM controller as a function of speed and switching frequency.

Table 4-2 Memory consumption in the SRM controller

Contents	Speed (RPM)								
	500	1000	2000	3000	4000	5000	6000	7000	8000
Switching Frequency (kHz)	18	19.8	20	21	21.6	22.5	23.2	24	25
Degrees per PWM Cycle	2	2	4	6	7	8	10	11	12
Bytes per Digit	1	1	1	1	1	1	1	1	1
Speed Granularity (RPM)	50	50	100	100	100	200	200	500	500
Memory per Speed Value (kB)	80	98	72	53.2	32.4	21	14.8	8	3
Memory per Speed Range (kB)	800	980	720	532	324	105	74	16	6
Total Memory Space Consumption = 3557 kB									

In order to obtain the expected torque ripple, all PWM cycles have been calculated over varying speed ranges. The switching frequency is adjusted based on the variation of speed, wherein the value is calculated in order to save memory as much as possible, and at the same time, to allow abundant detail for torque ripple minimization. The degrees distributed for one PWM cycle at different speeds are determined based on the minimal requirement for best torque ripple generation. Depending on the available

memory versus desired torque ripple, the degrees per PWM cycle and speed range are chosen, to meet the demand in different speed ranges. It is worthwhile mentioning here that the torque ripple is much more sensitive to the voltage-profile detail at low speed, whereas back-EMF is the critical concern at high speeds. According to the decided PWM cycle and speed granularity, it obvious that more memory space is occupied at low speeds compared to high-speed operation. For the tests conducted in the laboratory, the total consumed memory space amounts to 3557 kB, which is a reduction of about 70% memory space.

4.5 SUMMARY

This chapter introduced a novel voltage-profile algorithm, which can be used to calculate the SRM torque ripple and compute the corresponding phase voltage-profile. In order to deal with the high non-linearity, a finite approximate approach (Newton Method) is employed to organize an iterative calculation. In order to obtain the desired torque ripple level, the relationship between the processed voltage-profile and the yielded torque are established, based on applied phase current. The entire procedure is divided into two parts: the preparation part and the iterative calculation part. The former focuses on the voltage-profile initialization and preparation work for the iteration, while the latter is the iterative program, which is used to calculate the resultant torque ripple, based on the obtained voltage-profile. If the outcome is non-agreeable, the voltage-profile can be adjusted by a small variation, and the torque ripple will be recalculated and compared with previous results. The iteration stops either when it reaches the upper limit of the cycle time or if it obtains the desired torque ripple. Thereafter, the corresponding voltage-profile is stored into a look-up table.

In order to the reduce machine computational time and reduce program complexity, a calculated voltage-profile over different speeds is preferable. Based on the amount of hard calculation attempts, the critical parameters of the voltage-profile that affects the torque ripple at different rotor positions have been found. These parameters are classified as lateral and longitudinal variations.

This chapter also introduced the PWM cycle distribution approach to save memory. At first, the resultant voltage-profile is filtered and only two significant digits are retained after the decimal points. Thereafter, the data is re-recorded and only one data set is used to represent those unique sections. In addition, the PWM cycle is calculated over different speed ranges. The switching frequency is chosen between 18 kHz and 25 kHz, so as to eliminate the audible component as well as meet the control demand. Speed granularities are specified based on the requirement of the voltage-profile within the different speed ranges. Consequently, the total memory consumption is reduced.

CHAPTER 5
FPGA BASED OFF-LINE CONTROL DESIGN AND JTAG HARDWARE CO-SIMULATION

5.1 INTRODUCTION

Recently, there has been much interest shown in Field Programmable Gate Array (FPGA) controllers, due to rapid development of digital signal processing (DSP) technology and consistent industry demands. An FPGA is essentially an integrated circuit, which consists of a large number of logic gates and an embedded processor. Due to its on-board RAM feature, the FPGA is able to support immediate look-up table processes. Moreover, FPGAs can run at high frequency, up to 400 MHz, because of a high frequency system clock. This chapter discusses the use of a *Xilinx Virtex II Pro* FPGA as the central controller, to implement the optimized voltage-profile controller for the SRM drive. In addition, from the point of view of ambient operation, the overall system is developed in XSG coupling, within the MATLAB/Simulink environment, and all FPGA logic units are represented by Simulink sub-systems. Feedback information is received from an encoder, after which the controller starts searching for relevant voltage data inside the look-up table, stored in the on-board RAM. Thereafter, the resultant voltage data is compared with a saw-tooth waveform, in order to generate a PWM signal. Finally, the control signal is sent to the motor drive from the FPGA board.

As aforementioned, memory consumption is reduced to 3557 kB, due to PWM cycle distribution and reconfiguration of the special position section. However, this

memory is still very large for the *Xilinx Virtex II Pro* FPGA with on-board RAM, by an amount of 2448 kB. Thus, a look-up table split system is required, before carrying out the control operation. Based on the memory consumption for each speed range, summarized in the previous chapter, the look-up table for the entire speed range is divided into 18 parts. In this case, a dedicated look-up table for each separated speed range block is able to meet the size of the on-board RAM. In addition, due to the SRM operating principle, power stored in the phase winding will be returned back to the power source, during the de-energization period. Since only the motoring mode of the SRM is considered, a dumping system is utilized, which consists of a controlled switch and a large resistor, to protect the source from voltage spikes. When the DC bus voltage is beyond the upper limit, the dumping switch turns on, and the excess power is consumed by the resistor.

In this chapter, a JTAG based hardware co-simulation is implemented via the SRM drive control system, and the results are recorded using Matlab/Simulink. The overall system is divided into 3 stages: motor and drive stage, control preparation stage, and FPGA control logic stage. Torque ripple minimization for different speed ranges is implemented in hardware co-simulation environment, and the result is compared with classic fuzzy logic control technique, for high-speed operation. Furthermore, in order to verify the practical performance of the controller, the urban dynamometer driving schedule (UDDS) drive cycle is employed, and motor/controller operation efficiency for urban EV driving is evaluated.

5.2 XILINX VIRTEX II PRO FPGA AND XSG DEVELOPMENT TOOL

As is well known, an FPGA is primarily a semiconductor device, consisting of a large number of logic gates and a programmable routing resource as well as embedded processor, with an on-board RAM. An FPGA is able to implement custom designed combinational and sequential logic functions [56], [57]. Moreover, the processing capability of an FPGA is beyond that of a DSP. An FPGA typically depicts fast response time at controllable input and output (I/O) [57]. In addition, an FPGA works well with large look-up tables (LUTs), which are logic cells that ensure signal routing and tracking as well as one which enables fast data processing and analysis. Each LUT contains a number of digits, which can be invoked and programmed by the FPGA chip directly. Therefore, based on its powerful programmability and data processing ability, the FPGA is competent enough to meet the stringent requirements of voltage-profile based control technique. In particular, the *Xilinx Virtex II Pro* FPGA presents a number of attractive numerical features, including 30816 logic cells, 136 18-bit multipliers, 2448 kB of block RAM, and 2 PowerPC processors as well as a USB connector, for hardware co-simulation [58]. A concise overview of the critical components on the *Virtex II Pro* development board is depicted in Fig. 5-1 [57].

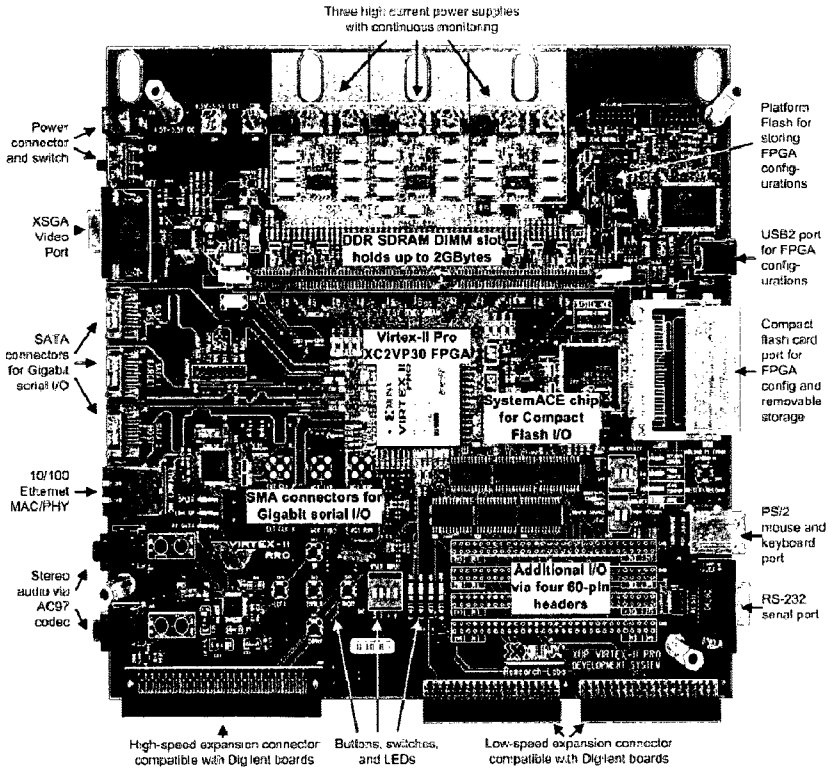

Fig. 5-1 *Xilinx Virtex II Pro* FPGA development board

The SRM drive system is developed in the Simulink environment, in order to implement the FPGA based hardware co-simulation. A visualized design tool, called XSG, is used. XSG is a DSP design tool, offered by *Xilinx*, that enables the use of model based Simulink, in Matlab, for FPGA design. Simulink has been extended by specific *Xilinx* block-sets, to provide a modeling environment that is suited to hardware design [59], [60]. Since other models are available in Simulink, those block-sets are divided into different libraries based on their function, including the *Xilinx* block-set, *Xilinx* reference block-set, and the *Xilinx* XtremeDSP kit. Through a good user interface, this tool allows access to low-level construction design, by using high-level resources and facilities, offering high efficiency and reliable FPGA design [61]. The XSG is an advanced development tool, which is able to translate each *Xilinx* block used in Simulink into hardware description language (HDL). Thus, experience with register transfer level (RTL)

design and VHSIC hardware description language (VHDL) are not required [59]-[61]. Thus, the system generator makes the FPGA based hardware co-simulation easily implementable in the Simulink environment.

5.3 FPGA BASED VOLTAGE-PROFILE CONTROLLER DESIGN

The major issue with conventional control techniques is that the current profile is difficult to regulate, due to significant DC bus voltage rise. Turn-on and Turn-off angle strategies are not able to maintain conduction time as desired. A trivial online controller cannot deal with the torque ripple issue for high-speed operation. Hence, a novel voltage profiling based off-line controller is proposed.

In order to establish a desired current profile, especially at high speeds, high frequency switching is required. In addition, a suitably sized look-up table is needed, in order to load the best torque ripple generation, based on feedback information. Therefore, in this thesis, a *Xilinx Virtex II Pro* FPGA is employed, to control each switch within the SRM drive. The layout of the entire control system is shown in Fig. 5-2. As is obvious, compared to the conventional method, described in the previous section, the current loop is eliminated. Furthermore, the turn-on and turn-off angle control is also abolished. Thus, the general complexity of the motor drive controller is reduced and overall stability of the system is increased. Hence, overall system dynamic response is improved.

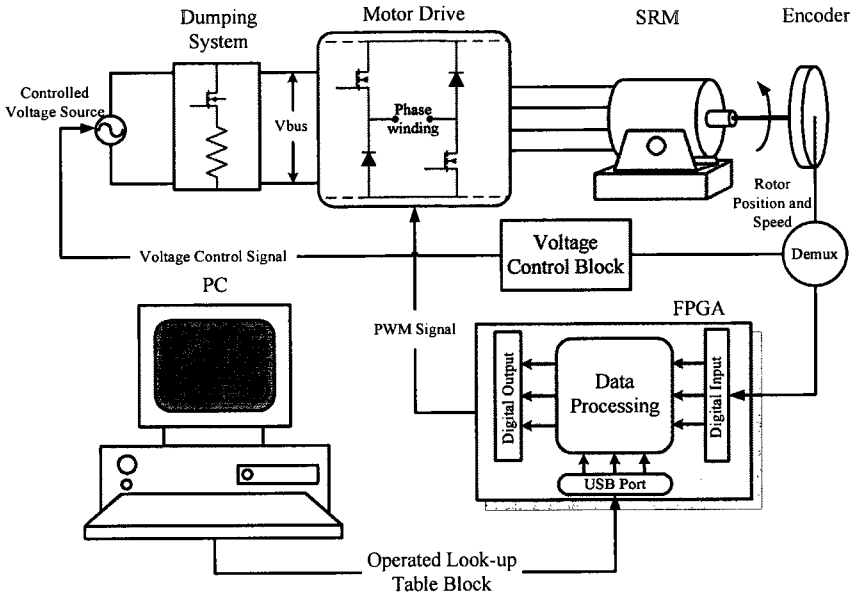

Fig. 5-2 FPGA based voltage-profile control system

Angular velocity and rotor position information is fed back into the FPGA, which yields a PWM signal to the drive, based on the voltage profiling look-up table, from a computer. The controlled voltage source is driven by a control block, based on the feedback information. During data processing, feedback information is also employed as an index, to find the corresponding voltage profile inside the look-up table, and hence, generate the desired PWM signal. Thus, the overall torque ripple is controlled to an acceptable level, by running the motor at an optimized voltage.

To avoid a voltage surge during de-flux period, due to the reverse flow of power, a dumping system, consisting of a controlled switch and a resistor are utilized. Fig. 5-3 describes the Simulink diagram of the dumping system, including a 1-D look-up table, which contains the maximum voltage for each speed range. The switch is controlled by comparing the upper limit voltage and the actual DC bus voltage. If the actual DC bus voltage is higher than the preset limit, the switch starts to conduct. Hence, excess power is consumed in the dump resistor.

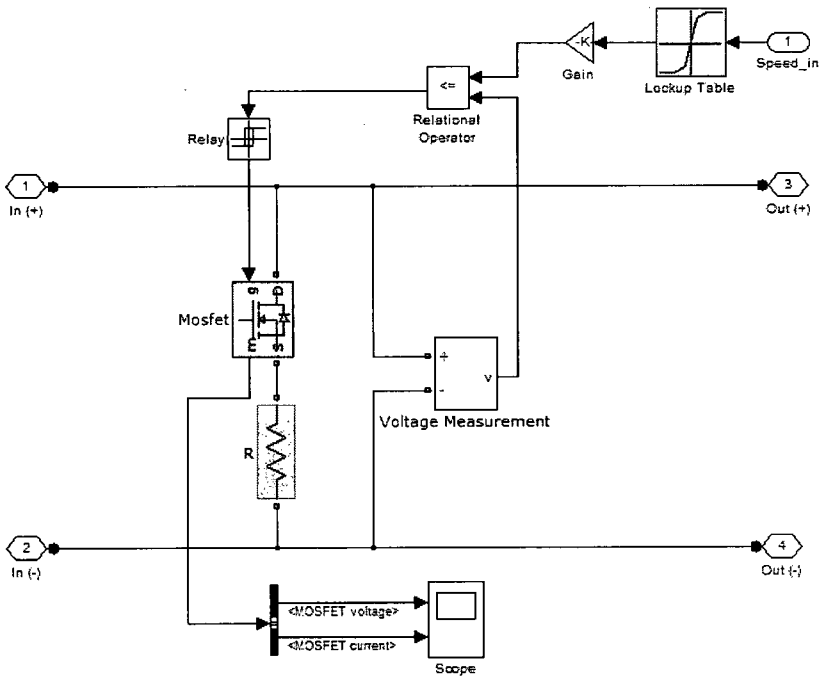

Fig. 5-3 Simulink diagram of the dumping system

As discussed in chapter 3, the tests are performed on a 7.5 kW, 8/6 SRM, whose torque-speed characteristic is shown in Fig. 5-4. Base speed for the test machine is 1200 rpm and the ultra-high speed range starts at 5800 rpm. This characteristic is modeled using the aforementioned current saturation method [62], [63]. With regards to the motor drive, as discussed in chapter 2, the classical SRM drive is utilized, consisting of two switches and two freewheeling diodes. In addition, it is worth re-iterating here that the SRM inductance profile was obtained through an experimental setup, which makes the test results more practical and reliable.

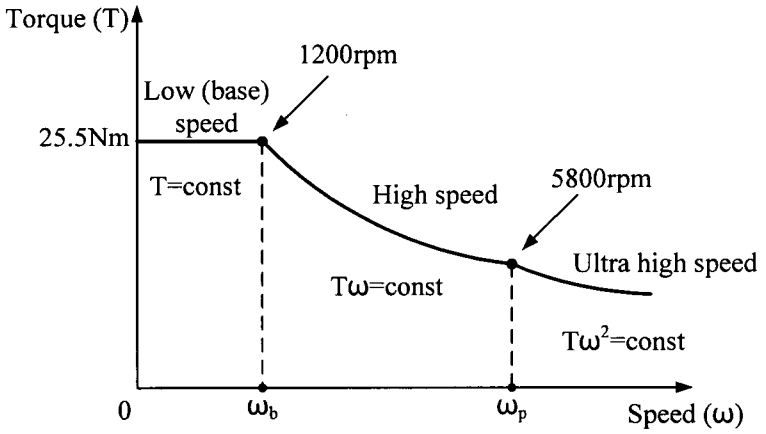

Fig. 5-4 Torque-speed characteristic of the test SRM

In view of the limitation of the on-board RAM, the huge information from the look-up table is divided and stored, before performing FPGA control. The Simulink/XSG layout of the look-up table split and storage system is presented in Fig. 5-5, where a number of small blocks are yielded from the original table, based on memory usage, as discussed in the previous chapter. With the help of the condition block, the original look-up table is divided into 4 parts, based on different speed regions. Thereafter, each region starts to break into smaller blocks, which contain much less information. Inside each action block, the sub look-up tables are yielded, based on memory consumption in each speed range, so that all sub look-up tables are able to fit into the on-board RAM. Due to less information in the ultra high speed range, only 1 sub look-up table (action block 4) proves to be sufficient. Based on speed information from the encoder, the current operated look-up table is selected and uploaded on to the on-board RAM. Fig. 5-6 depicts the details of the XSG model for the FPGA storage system.

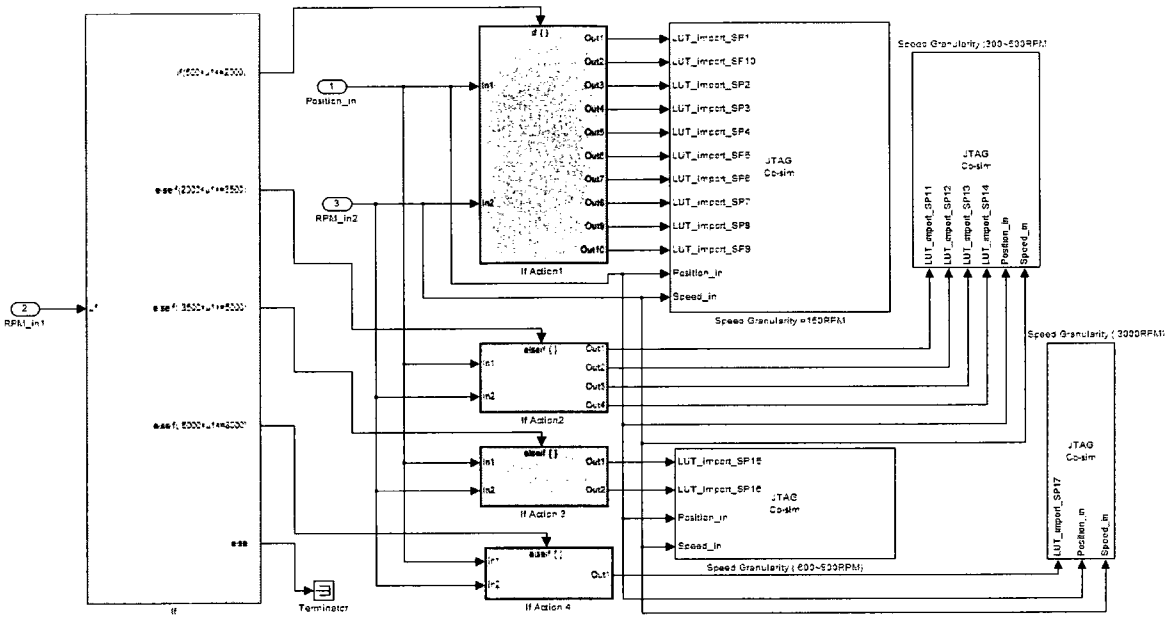

Fig. 5-5 Simulink/XSG model of the look-up table split and storage system

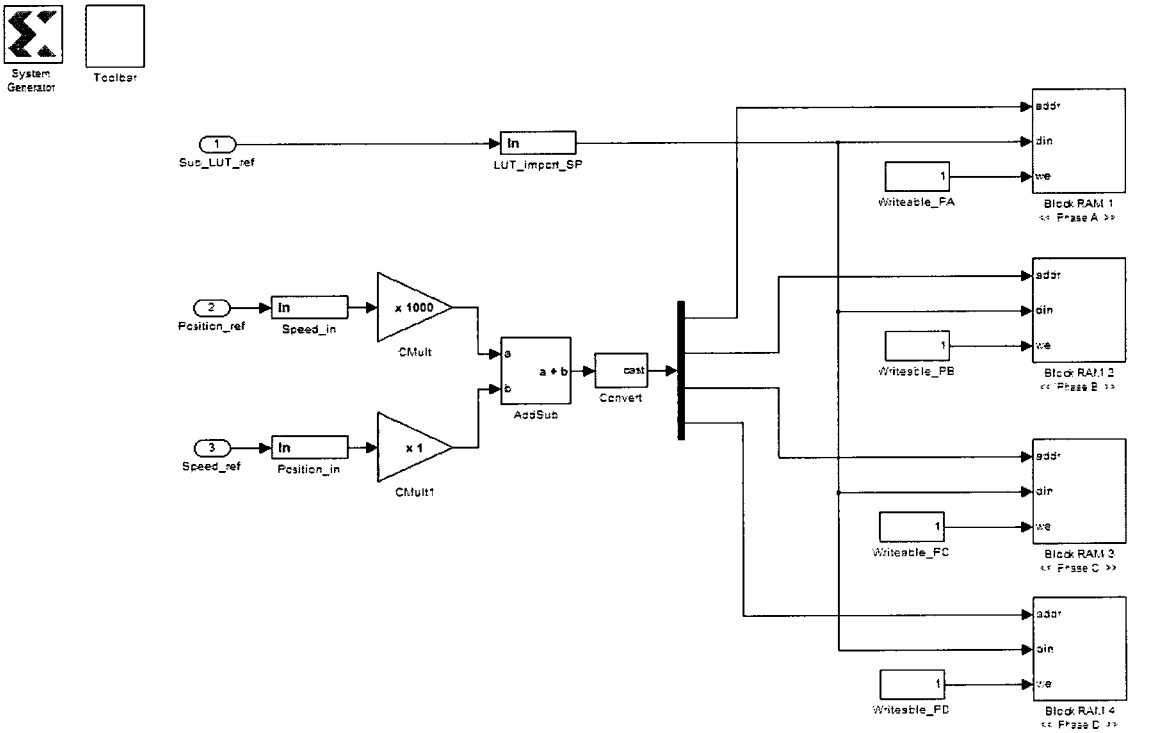

Fig. 5-6 XSG model of the FPGA storage system

With regards to the FPGA storage system, 4 block RAMs are assigned to each look-up table, so as to represent each phase of the test SRM. A unique address is

generated by different gains, to receive instantaneous speed and position information. In order to ensure that all on-board RAMs function properly, the writeable function has to be checked and the depth for each block RAM has to be defined logically. Furthermore, the access mode of the memory has to be defined as write only. The data inside the current operated table is automatically stored into the block RAM, assigned with a compound address. Finally, the data is uploaded on the FPGA, for further processing.

During the on-board processing period, the data is invoked by referring to the compound address. Fig. 5-7 depicts the XSG model of the FPGA data processing system.

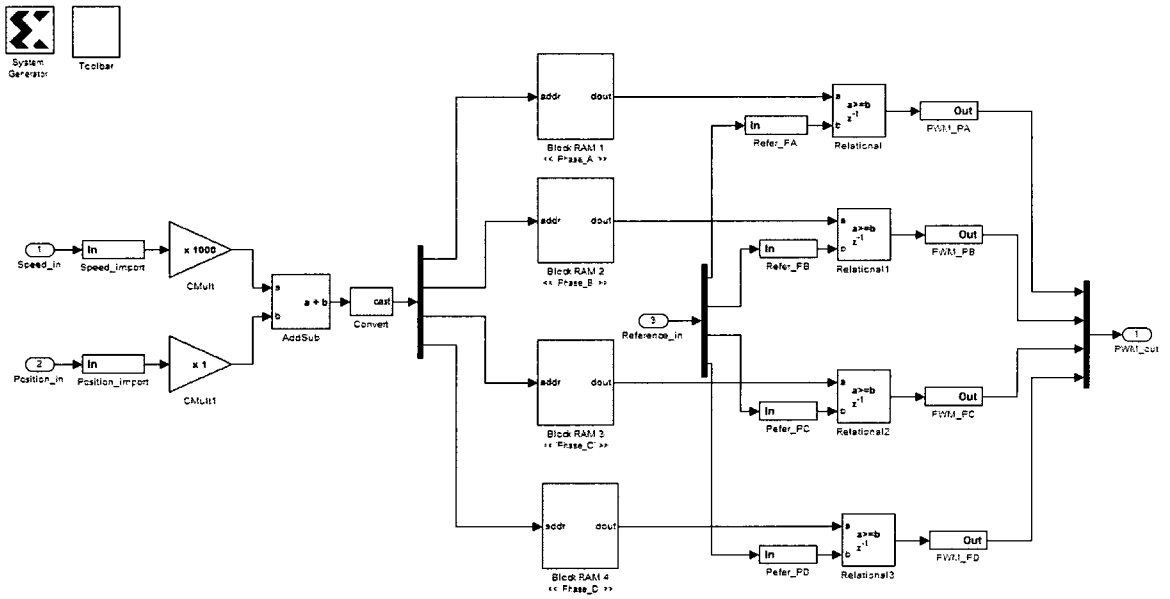

Fig. 5-7 XSG model of the FPGA on-board processing system

In order for the data to be readable, the access mode of the block RAM has to be defined as read only. Through the relational block, the value of the data is compared with an estimated triangular waveform, whereby suitable PWM signals are yielded for each phase of SRM. Hence, the semiconductors in the motor drive are controlled by optimized voltage-profile based PWM signals.

5.4 JTAG Based Hardware Co-Simulation Results and Performance Analysis

The practical tests are performed by implementing the voltage-profile control algorithm in Matlab/Simulink. All logic cells used in the FPGA are represented by the XSG tool, to allow execution of JTAG hardware co-simulation. The setup for hardware co-simulation is depicted in Fig. 5-8.

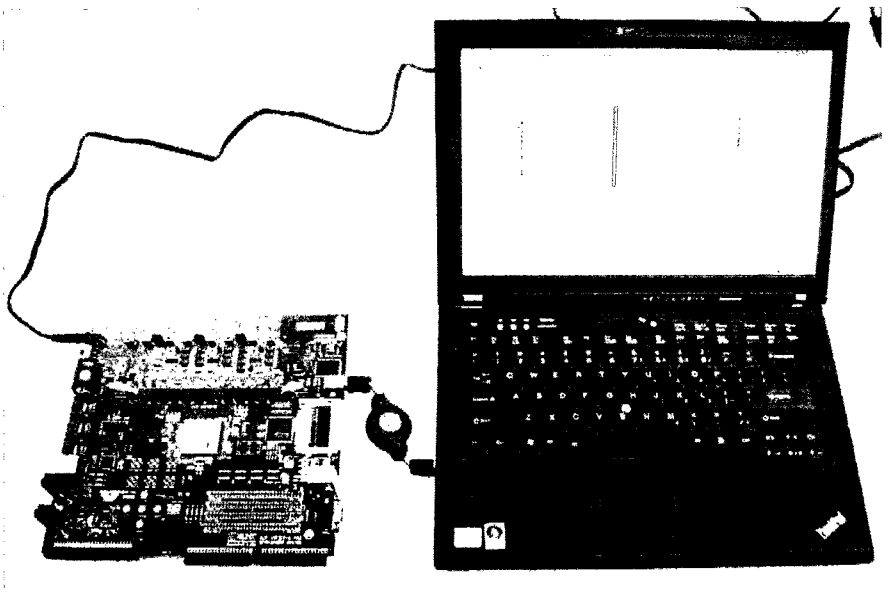

Fig. 5-8 Test setup for JTAG hardware co-simulation

At first, the conventional torque ripple minimization technique is compared with the proposed novel approach. Thereafter, the generated torque ripple for different speeds is explored, and the results are analyzed.

5.4.1 Comparative Test Results

The current profile based torque ripple minimization method is established based on the conventional technique, described in chapter 2. The turn-on and turn-off angles are readjusted, based on the instantaneous testament and the operated voltage and current are

shown in Fig. 5-9 (a). The results are recorded and calculated, while the motor was running at 1500 rpm. The resultant torque ripple is generated and presented in Fig. 5-9 (b). The total torque ripple is about 20.03%. Referring to the torque-speed characteristics, it is obvious that the motor is running in the constant power range, higher than the base speed of 1200 rpm.

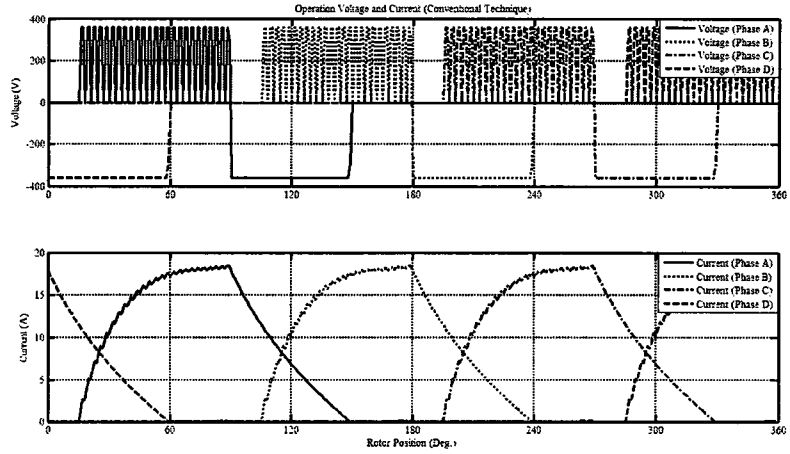

(a) Applied voltage-profile and phase current

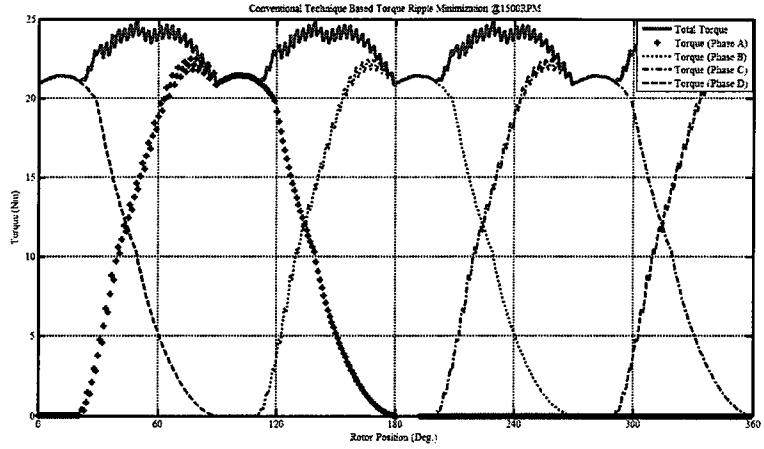

(b) Resultant phase torque and total torque

Fig. 5-9 Conventional torque ripple minimization technique

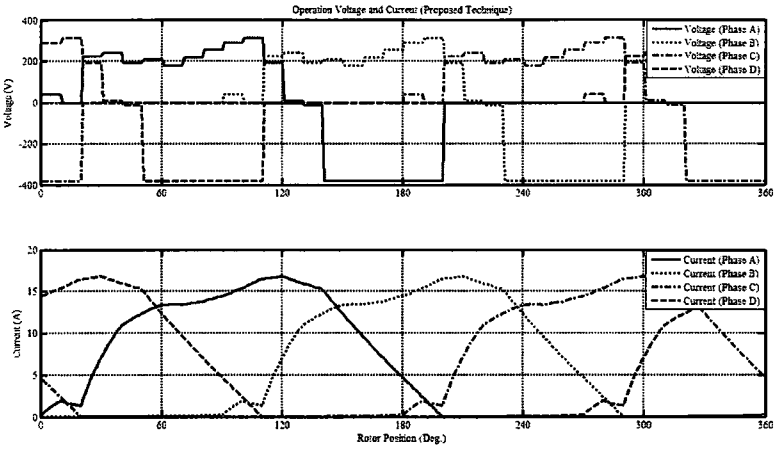

(a) Applied voltage-profile and phase current

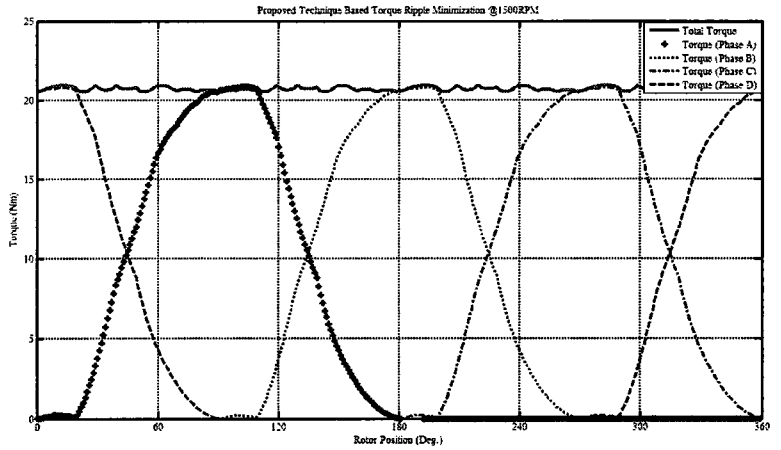

(b) Resultant phase torque and total torque

Fig. 5-10 Voltage-profile based torque ripple minimization

Based on the precisely modeled inductance profile, the optimized voltages are obtained using Matlab, and are registered in a speed-position-voltage based 3-D look-up table. While running the motor, the FPGA receives feedback information, including rotor position and angular velocity. A PWM signal is generated as long as a voltage profile is obtained. When the SRM runs at 1500 rpm (high-speed), the applied voltage profile and the obtained phase current are as depicted in Fig. 5-10 (a). The yielded phase torque as well as total torque is presented in Fig. 5-10 (b). In this case, the resultant torque ripple is a mere 2.17%, which is highly satisfactory.

5.4.2 VOLTAGE-PROFILE BASED TORQUE RIPPLE MINIMIZATION

The tests are performed by JTAG hardware co-simulation and recorded in Matlab workspace. The overall system layout in Simulink/XSG environment is shown in Fig. 5-11. To verify the performance of the proposed approach, the torque ripples produced at different speed values are plotted respectively. Fig. 5-12 (a) depicts motor operation in the base speed range (at 800 rpm), whereby the obtained resultant torque-ripple is less than 2%. Fig. 5-13 (a) depicts motor operation in high speed range (at 3000 rpm), whereby the obtained resultant torque-ripple portrays a low value, of about 2.3%. When the motor operates in the ultra high speed range (at 7000 rpm), the torque ripple is still acceptable, at about 2.7%, as shown in Fig. 5-14(a).

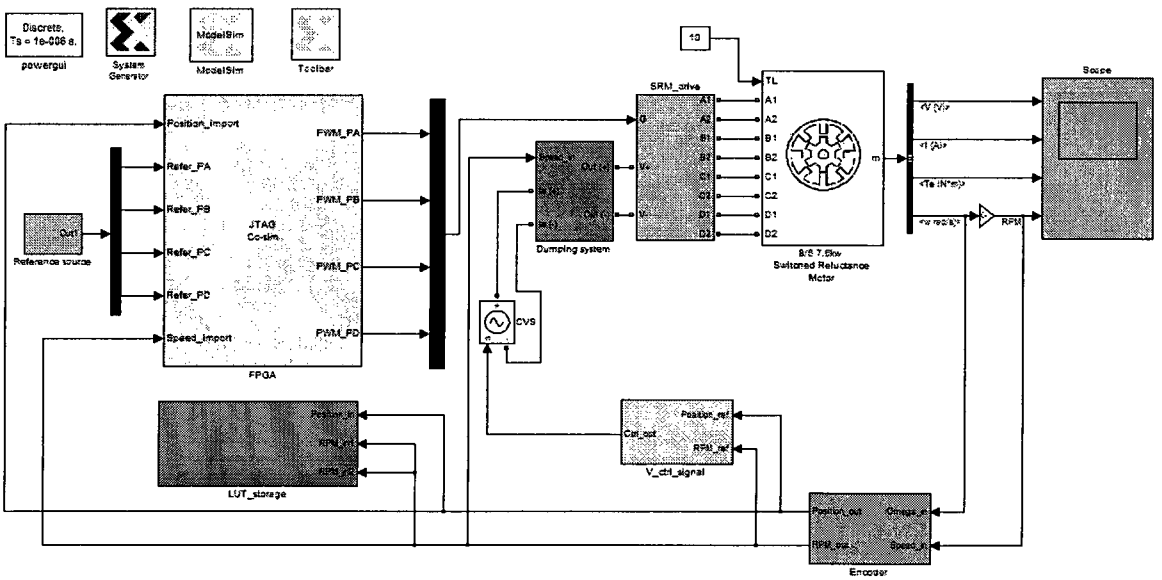

Fig. 5-11 Simulation/XSG model of the overall system

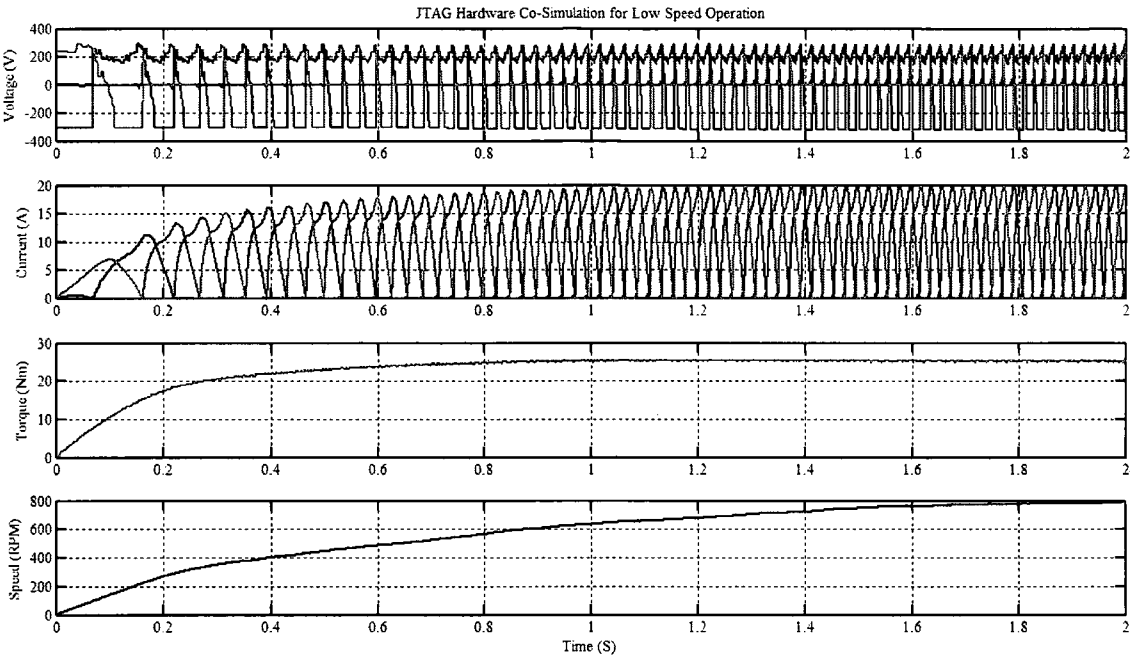

(a) Time based operation @800 rpm

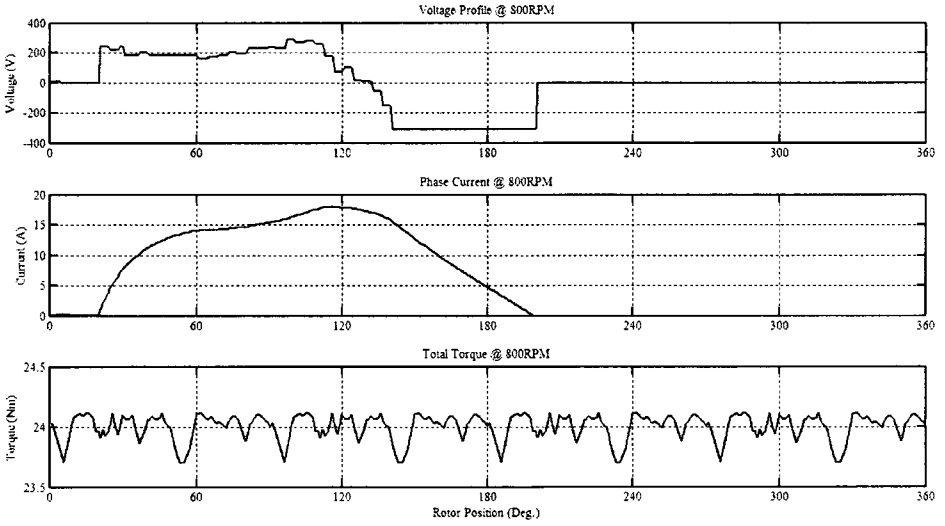

(b) Position based operation @800 rpm

Fig. 5-12 Voltage-profile technique, operating at base speed

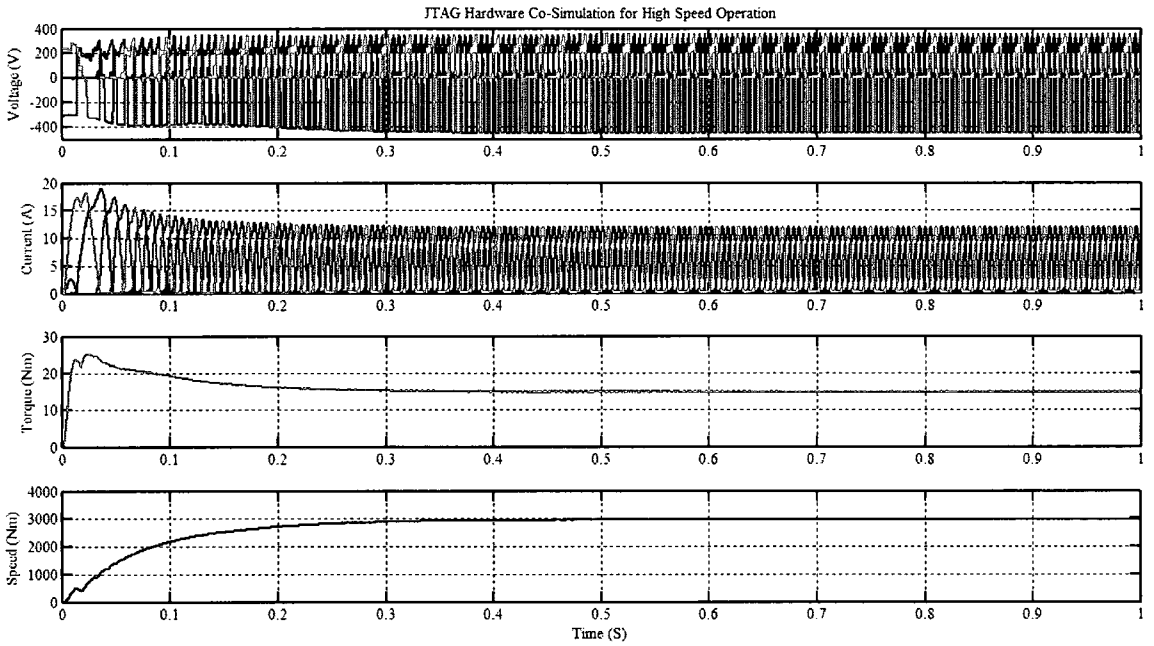

(a) Time based operation @3000 rpm

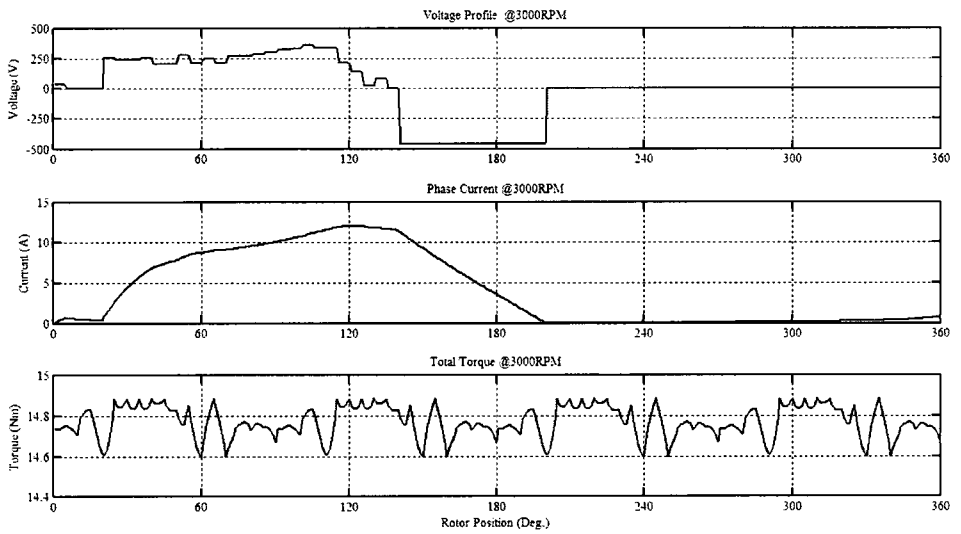

(b) Position based operation @3000 rpm

Fig. 5-13 Voltage-profile technique, operating at high speed

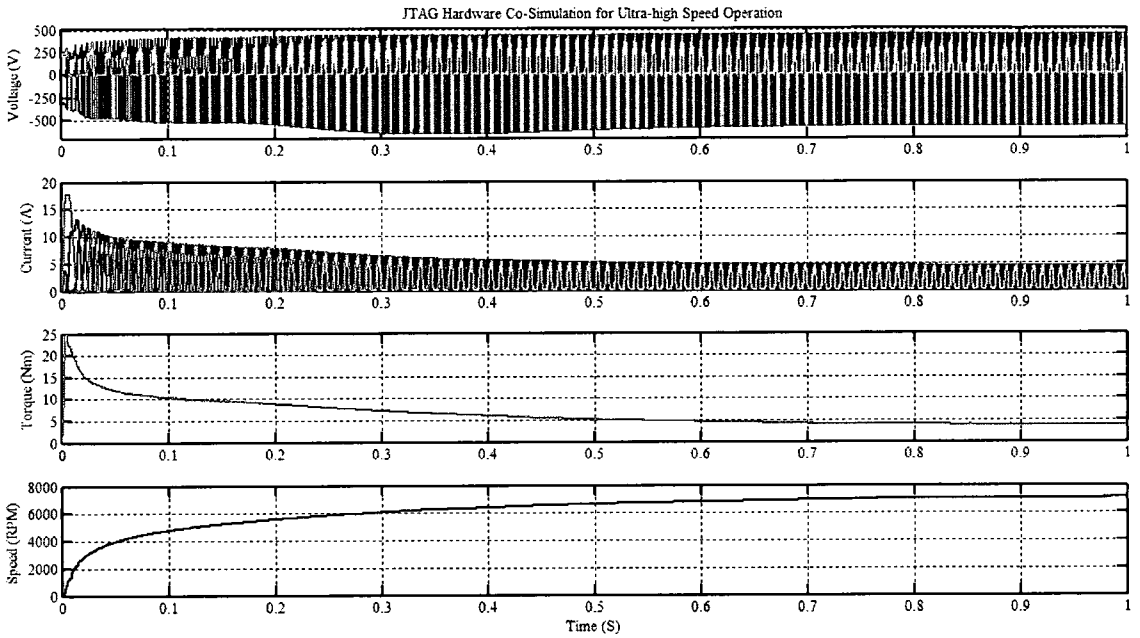

(a) Time based operation @7000 rpm

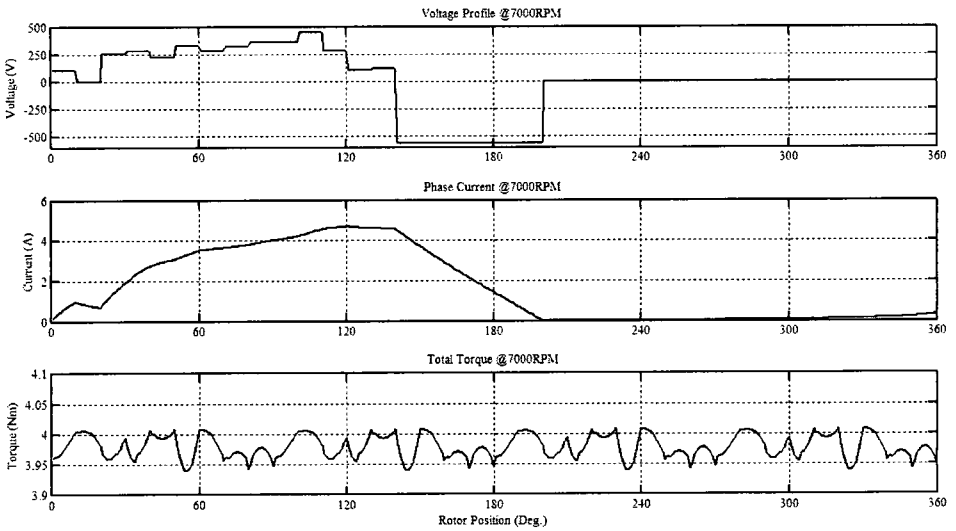

(b) Position based operation @7000 rpm

Fig. 5-14 Voltage-profile technique, operating at ultra-high speed

Details of the voltage-profile, applied current, and resultant torque ripple in one phase, over one electrical degree period, for low speed, high speed, and ultra-high speed are depicted in Figs. 5-12 (b), 5-13 (b), and 5-14 (b), respectively.

5.5 FPGA BASED SRM PROPULSION SYSTEM OPERATING UNDER THE UDDS DRIVE CYCLE TEST

As an additional practical test, the modeling of the target SRM based propulsion system is carried out in Matlab/Simulink, by referring to the Advanced Vehicle Simulator (ADVISOR) software [64], [65]. The developed SRM based EV propulsion system is tested for city driving performance. In order to verify the performance of the overall system, the UDDS driving schedule is used as reference speed. UDDS driving data is compared with sensed motor rotation speed after being adjusted, and the layout of the overall system is shown in Fig. 5-15. In order to analyze the overall efficiency of the motor/controller operation in traction mode, the test is performed by implementing the control system in the developed SRM based propulsion system model.

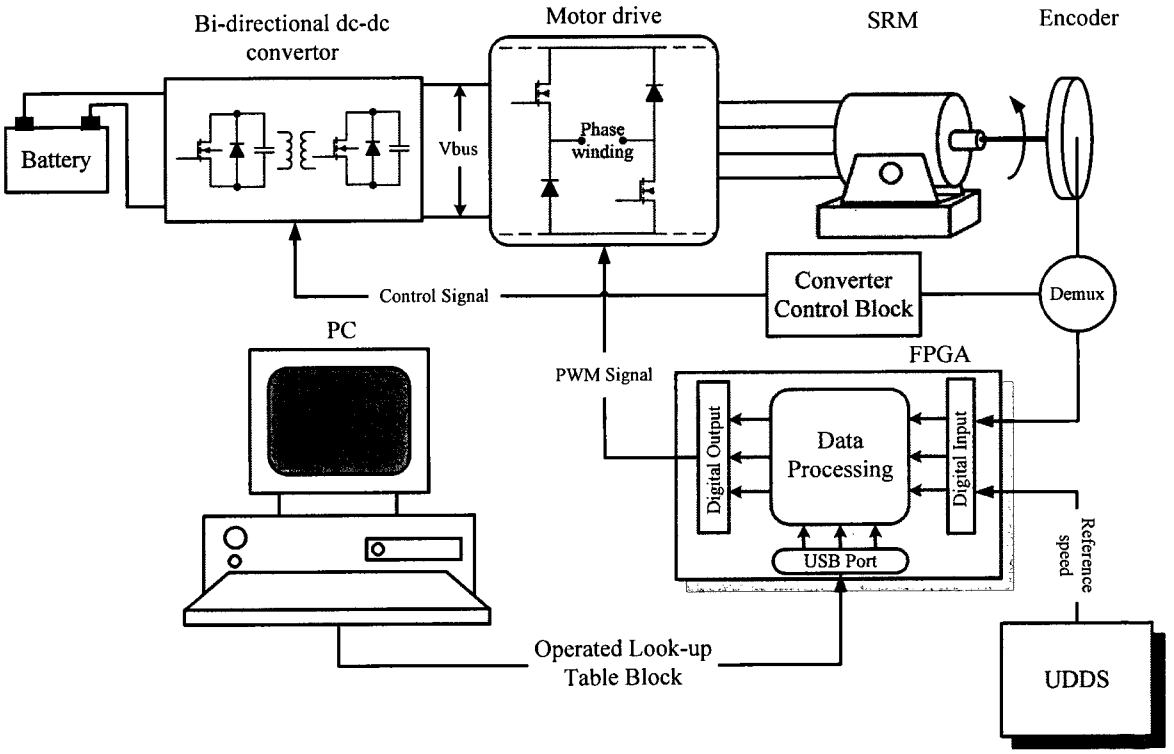

Fig. 5-15 FPGA based SRM propulsion system under UDDS drive cycle test

The collected data and the target SRM model are injected into the pre-built propulsion system model, so that the motor efficiency can be observed. In addition, the simulation time is extended to 10 seconds, in order to verify the stability of the motor drive control, due to expanded operating points. Fig. 5-16 (a) illustrates the comparative test results between the referred UDDS drive schedule and the obtained rotation speed of the SRM. Corresponding voltage, current, and torque are depicted in Fig. 5-16 (b). Furthermore, the efficiency of the traction motor versus the simulation period is shown in Fig. 5-16 (c).

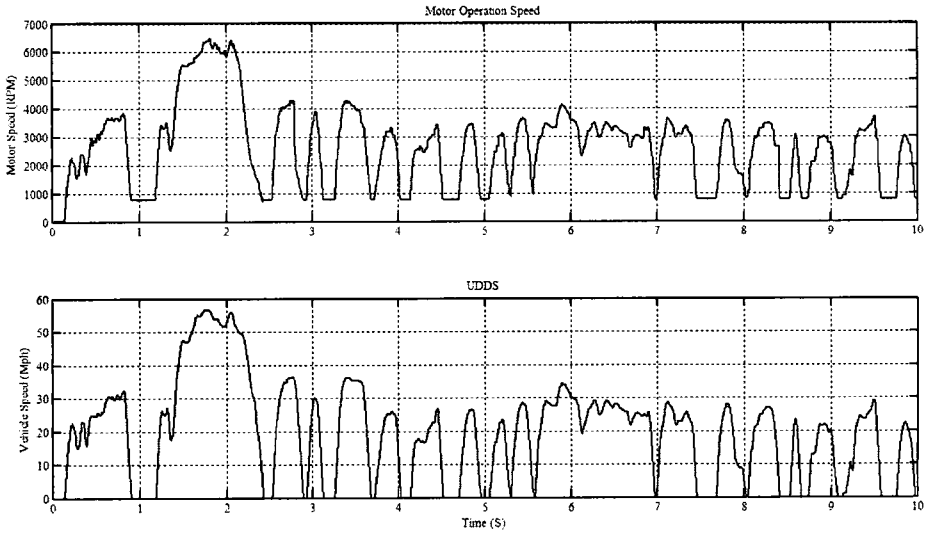

(a) Comparison between motor speed and UDDS driving pattern

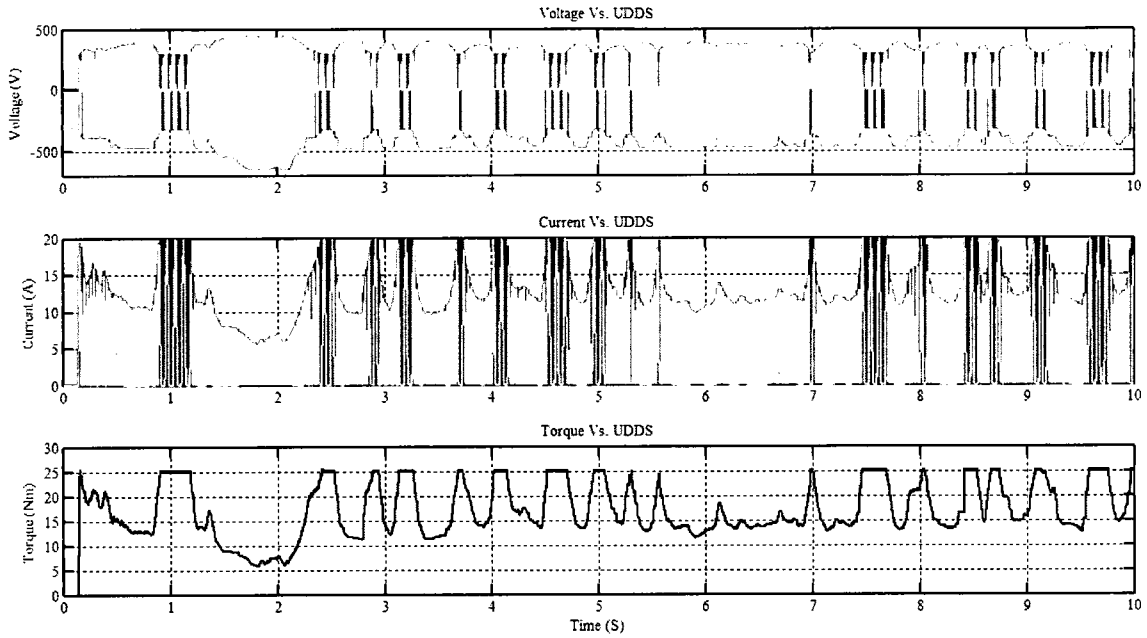

(b) Operating voltage, current, and torque under UDDS test

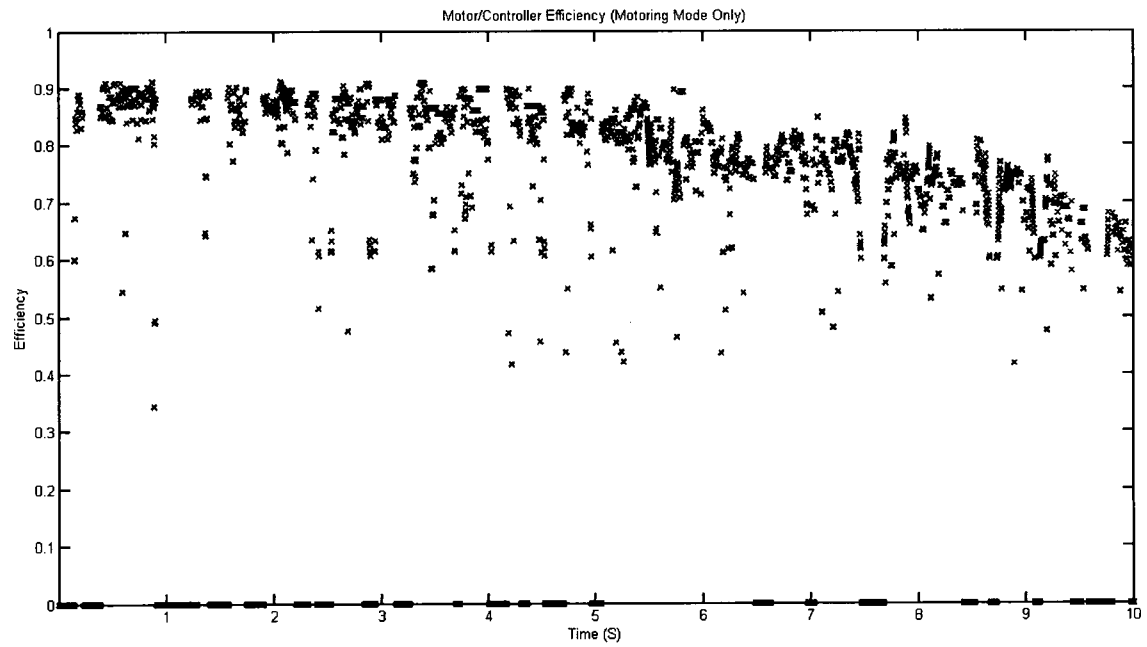

(c) Motor/controller efficiency map

Fig. 5-16 Motor/controller performance under UDDS drive cycle test

According to Fig. 5-16 (a), the resultant speed is very close to reference speed. The highest speed of the SRM (around 6000 rpm) appears while the HEV achieves its highest speed (56.7 mph). However, the rotating speed could be higher than the real case. As aforementioned, the SRM is mounted on the same shaft with ICE in the ISA driving train system, the idle rotation speed of the traction motor is necessary to be defined. The operation voltage, current and the resultant torque is presented in Fig. 5-16 (b). Due to the fact that the system is tested for urban driving, the traction motor (SRM) always works in the low speed range, with low efficiency. Hence, the motor controller efficiency is low during motoring mode, which is around 65%-85%, as seen in Fig. 5-16 (c). Moreover, it is important to note that the purpose of this thesis is to minimize the torque ripple over the entire speed range, which means the max power efficiency of the motor cannot be achieved at the same time, therefore the trade off should be concerned.

5.6 SUMMARY

Based on specific system requirements, the FPGA is employed as a controller in order to drive the test SRM. This chapter introduced the *Xilinx Virtex II Pro* FPGA and the XSG block-set based development tool. The basic features as well as advantages were highlighted. The layout of the FPGA based voltage-profile control system was presented, and the design principle was described. The torque-speed characteristic of the test SRM was presented, and the critical components inside the control system, including the dumping system, the look-up table split, and storage system as well as the FPGA on-board processing system, were explored in detail. Furthermore, the Simulink/XSG diagram for each system was illustrated and the operation procedure was studied.

The overall system was run under JTAG based hardware so-simulation, and the logic cells on the FPGA board were represented by XSG blocks, which are interactively connected with virtual blocks in Simulink. At first, simulation results were compared between the conventional technique and the voltage-profile technique. Torque ripple results suggest that the proposed technique has better overall performance, even at high speeds. The operation voltage, current, and torque for different speed were studied. It was observed that torque ripple is mostly suppressed below 3% over the entire speed range. In addition, the UDDS driving schedule is introduced as a speed reference to verify the performance of the FPGA based SRM propulsion system for a real EV application, running in city driving conditions. The operation status was recorded and the motor/controller overall efficiency was calculated.

CHAPTER 6

CONCLUSIONS

6.1 SUMMARY

In order to improve the overall efficiency of an EV/HEV propulsion system, an ISA system that combines the function of engine start and on-board generation. Such an ISA based EV propulsion system is studied in the initial part of this thesis. The three prime motor candidates for ISA applications, in the form of IM, PMSM, and SRM are studied and compared. Due to its excellent wide speed range features, the SRM is regarded as the best ISA machine option. However, high torque ripple is a serious issue in SRMs. Moreover, SRMs also depict highly non-linear characteristics. Hence, the objective of this thesis, firstly, was to accurately model the SRM non-linear characteristics. Secondly, a novel controller was designed and developed for an SRM based EV propulsion system, so as to suppress torque ripples over the entire speed range.

The initial part of the thesis explained the basic topology of an 8/6 SRM. Conventional torque ripple minimization control techniques, such as the classic current hysteresis control and turn on/off angle control were discussed. However, conventional techniques are unable to suppress torque ripple in the high-speed range, due to the limitation of the DC bus voltage. This is mainly due to significant rise in back-EMF at high speeds, which restricts the wide speed range operation of SRM.

Thus, in order to enhance motor performance, an accurate model coupled with an appropriately designed control strategy is critical. Normally, the performance of an SRM

is studied through its magnetization curve for different rotor positions and applied phase currents. Compared to conventional methods, the proposed novel method uses a low-frequency switching signal. Thus, the copper losses are more dominating, and a resistive voltage drop, rather than phase voltage, is calculated. In addition, since the proposed method uses a one-switch, one-diode topology, the overall set-up is quite uncomplicated and highly specific devices are not necessary. A numerical filter was designed to address interference noises introduced by electrical devices. Hence, the yielded experimental results were precise and reliable. In order to verify the accuracy of each method, FEA based simulation results were used as a reference and compared with the results yielded by other methods, in both aligned and unaligned position. It was observed that the results obtained by the proposed current saturation method were closest to the FEA results, and hence, a much more accurate inductance model was obtained for the test SRM.

The accurately developed inductance model information was used for a novel voltage-profile algorithm, based on a finite approximation approach (Newton method). The developed technique is used to calculate the possible voltage-profiles through different current values. Referring to the operating principle of an SRM, the relationship between the voltage profile and the resultant torque is established through phase current. The voltage-profile is stored in a look-up table, while the expected torque ripple level is achieved. Otherwise, the iteration program applies a predefined verification into the current voltage-profile and carries out the next calculation. Instead of directly carrying out the program, a calculated voltage-profile is preferable, so as to lower the machine time. By means of rudimentary calculations, it was found that the yielded torque ripple is affected by specific parameters, which can be classified as lateral variations and

longitudinal variations. Each parameter value is recorded over the entire speed range through tests. The initial voltage-profile is formed by adjusting the critical parametric values. A suitable PWM cycle distribution approach was described, in order to minimize overall memory consumption. At first, only one data is applied to represent a specific rotor position, in the voltage-profile. The implemented PWM cycle is eventually computed for each speed granularity. A specific data set is used to represent each cycle. Thus, the total space of occupied memory is reduced.

Then, with regards to the controller implementation and development environment, the *Xilinx Virtex II Pro* FPGA and the XSG block-set based Matlab/Simulink tool were utilized. According to the design procedure, the critical sub-systems, including the dumping system, look-up table split, and the storage system as well as the FPGA on-board processing system, were explored. The overall system was implemented under JTAG based hardware co-simulation, whereby the logic cells on the FPGA board were represented by XSG blocks, which are interactively connected with Simulink virtual blocks through a USB platform cable. The tests were performed on a 7.5 kW, OULTON 8/6 SRM, whose characteristics are observed through its torque-speed curve. The test results obtained by conventional control algorithms and the proposed approach are presented and compared. The resultant torque ripple over the entire speed range was explored, using the proposed voltage-profile technique. It must be highlighted that the torque ripple in all speed ranges was found to be below 3%.

Finally, the overall motor/controller efficiency was tested under UDDS urban drive schedule, and overall system performance was evaluated. It was observed that the torque ripple was suppressed to an acceptably low level, using the proposed technique.

6.2 SUGGESTIONS FOR FUTURE WORK

As part of future work, simplification of the voltage profile calculation is necessary. Moreover, the designed algorithm needs to be tested for various types of SRM drives. As is well known, the new generation of MOSFETs can easily operate at about 20 kHz (or even higher frequency). In order to implement the proposed technique practically, the voltage profiling method must depict compatibility with high-speed motor drives. Therefore, another aspect of potential future work could include semiconductor selection for the high-speed, high power motor drive setup.

With regards to the experimental setup, high power diodes need to be used, due to the significant negative voltage present at each de-flux period. Moreover, since the developed voltage-profile technique is highly dependent on feedback information, a good optical encoder, with high sensitivity, is needed. In order to protect the MOSFET in each phase, a well-designed resistor-capacitor (RC) snubber circuit could be a primary option, where the value of the resistor and capacitor are calculated based on the operation status. In addition, the entire motor drive could be mounted on a heat-sink, due to high power operation. Furthermore, ground must be well-isolated to avoid hazards due to short circuits. Finally, a specialized FPGA, with customized I/O terminals, available from *Opal-RT*, along with the development tool, *RT-Lab*, are preferable for future advanced experimental implementation and improvement of the developed technique.

REFERENCES

[1] C. C. Chan, "An overview of electric vehicle technology," *Proc. of the IEEE*, vol. 81, no. 9, Sept. 1993, pp. 1202-1213.

[2] R. D. Strattan, "The electrifying future of the hybrid automobile," *IEEE Potentials*, vol. 23, no. 3, Aug. 2004, pp. 3-7.

[3] C. C. Chan, "The state of the art of electric and hybrid vehicles," *Proc. of the IEEE*, vol. 90, no. 2, Feb. 2002, pp.247-275.

[4] T. H. Ortmerey and P. Pillay, "Trends in transportation sector technology energy usage and greenhouse gas emission," *Proc. of the IEEE*, vol. 89, no.12, Dec. 2001, pp.1837-1847.

[5] P. Zhang and S. S. Williamson, "Status review of integrated starter-alternator based hybrid electric vehicle drive trains," in *Proc. IEEE Vehicle Power and Propulsion Conf.*, Harbin, China, Sept. 2008, pp.1-8.

[6] W. Cai, "Starting engines and powering electric loads with one machine," *IEEE Industry Applications Magazine*, vol. 12, no. 6, Nov. 2006, pp. 29-38.

[7] S. S. Williamson, A. Khaligh, and A. Emadi, "Impact of utilizing selective motor topologies and control strategies on the overall performance of integrated starter alternator (ISA) based HEVs," in *Proc. IEEE International Electric Machines and Drives Conf.*, Antalya, Turkey, May 2007, pp. 134-139.

[8] A. Emadi, S. S. Williamson, and A. Khaligh, "Power electronics intensive solutions for advanced electric, hybrid electric, and fuel cell vehicular power systems," *IEEE Trans. on Power Electronics,* vol. 21, no. 3, May 2006, pp. 567-577.

[9] M. Douba, H. Ng, and R. Larson, "Characterization and comparison of two hybrid electric vehicles (HEV)—Honda Insight and Toyota Prius," in *Proc. SAE World Congress and Exhibit*, Detroit, MI, Mar. 2001.

[10] I. Boldea, "Starter/alternator system for HEV and their control: a review," *KIEE Int. Trans. EMECS,* vol. 4-B, no. 4, pp.157-169, July 2004.

[11] A. Emadi, B. Fahimi, M. Ehasni, and J. M. Miller, "On the suitability of low-voltage (42V) electrical power systems for traction applications in parallel hybrid electric vehicles," in *Proc. SAE Future Car Congress*, Arlington, VA, April 2000.

[12] A. Emadi, K. Rajashekara, S. S. Williamson, and S. M. Lukic, "Topological overview of hybrid electric and fuel cell vehicular power system architectures and configurations," *IEEE Trans. on Vehicular Technology*, vol. 54, no. 3, pp. 763-770, May 2005.

[13] K. Rajashekara, "42V architectures for automobiles," in *Proc. IEEE Electrical Manufacturing and Coil Winding Expo.*, Indianapolis, IN, Sept. 2003, pp. 431-434.

[14] P. Nicastri and H. Huang, "42V PowerNet: providing the vehicle electrical power for the 21st century," in *Proc. SAE Future Transportation Technology Conf. and Expo.*, Costa Mesa, CA, Aug. 2000.

[15] W. Cai, "Comparison and review of electric machines for integrated starter alternator applications," in *Proc. IEEE 39th Annual Industry Application Conf.*, Oct. 2004, vol. 1, pp. 386-393.

[16] S. Chen, B. Lequesne, R. R. Henry, Y. Xue, and J. J. Ronning, "Design and testing of a belt-driven induction starter-generator," *IEEE Trans. on Industry Applications*, vol. 38, no. 6, pp. 1525-1533, Dec. 2002.

[17] T. M. Jahns, "Torque production in permanent magnet synchronous motor drives with rectangular current excitation," *IEEE Trans. on Industry* Applications, vol. IA-20, no. 4, pp. 803-813, July/Aug. 1984.

[18] E. C. Lovelace, T. M. Jahns, T. A. Keim, and J. H. Lang, "Mechanical design considerations for conventionally laminated, high-speed, interior PM synchronous machine rotors," *IEEE Trans. on Industry Applications*, vol. 40, no. 3, pp. 806-812, June 2004.

[19] E. C. Lovelace, T. M. Jahns, J. L. Kirtley Jr, and J. H. Lang, "An interior PM starter/alternator for automotive applications," in *Proc. IEEE International Conf. on Electrical Machines*, Istanbul, Turkey, Sept. 1998, pp. 1802-1808.

[20] A. A. Abdallah, V. Devanneaux, J. Faucher, B. Dagues, and A. Randria, "Modelling of surface-mounted permanent magnet synchronous machines with stator faults," in *Proc. 30th IEEE Annual Conf. of the Industrial Electronics Society*, Nov. 2004, pp. 3031-3036.

[21] W. Cai, P. Pillay, and A. Omekanda, "Low vibration design SRMs for automotive applications using modal analysis," *IEEE Trans. on Industry Applications*, vol. 39, no. 4, pp. 971-977, Aug. 2003.

[22] M. Sanada, S. Morimoto, Y. Takeda, and N. Matsui, "Novel rotor pole design of switched reluctance motors to reduce the acoustic noise," in proc. *IEEE Industry Applications Conf.*, Oct. 2000, vol. 1, pp. 107-113.

[23] N. Inanc, A. Derdiyok, and V. Ozbulur, "Torque ripple minimization of a switched reluctance motor including mutual inductances via sliding mode control technique,"

in *Proc. IEEE International Symposium on Industrial Electronics*, July 1997, vol. 3, pp. 1024-1028.

[24] L. Venkatesha and V. Ramanarayanan, "Torque ripple minimisation in switched reluctance motor with optimal control of phase currents," in *Proc. IEEE International Conf. on Power Electronic Drives and Energy Systems for Industrial Growth*, Dec. 1998, vol. 2, pp. 529-534.

[25] N. C. Sahoo, J. X. Xu, and S.K. Panda, "Determination of current waveforms for torque ripple minimization in switched reluctance motors using iterative learning: an investigation," *IET Electric Power Applications*, vol. 146, no. 4, pp. 369-377, July 1999.

[26] T. K. Ha, C. H. Kim, J. H. Kim, S. Y. Pyo, and S. K. Lim, "Simple and high-performance drive of switched reluctance motors for low-cost applications," in *Proc. IEEE International Symposium on Industrial Electronics*, July 1997, vol. 2, pp. 631-636.

[27] R. Krishnan, "Switched Reluctance Motor Drives: Modeling, Simulation, Analysis, Design, and Application," CRC Press, Industrial Electronics Series, 2001.

[28] T. J. E. Miller, "Electronic Control of Switched Reluctance Machines," Newnes Power Engineering Series, 2001.

[29] M. Ehsani and I. Husain, "Torque ripple minimization in switched reluctance motor drives by PWM current control," *IEEE Trans. on Power Electronics*, vol.11, no. 1, pp. 83-88, Jan. 1996.

[30] N. C. Sahoo, J. X. Xu, and S. K. Panda, "Low torque ripple control of switched reluctance motors using iterative learning," *IEEE Trans. on Energy Conversion*, vol. 16, no. 4, pp. 318-326, Dec. 2001.

[31] Z. Z. Ye, T. W. Martin, and J. C. Balda, "Modeling and nonlinear control of a switched reluctance motor to minimize torque ripple," in *Proc. IEEE Conf. on Systems, Man, and Cybernetics*, Nashville, TN, Oct. 2000, pp. 3471-3478.

[32] N. Inanc, A. Derdiyok, V. Ozbulur, and Y. Ozoglu, "Optimal phase current profiling of SRM by fuzzy logic controller to minimize torque ripple," in *Proc. IEEE International Symposium on Industrial Electronics*, Istanbul, Turkey, July 1997, pp. 77-82.

[33] M. Divandari, A. Koochaki, A. Maghsoodloo, H. Rastegar, and J. Noparast, "High performance SRM drive with hybrid observer and fuzzy logic torque ripple minimization," in *Proc. IEEE International Symposium on Industrial Electronics*, Vigo, Spain, June 2007, pp. 1230-1235.

[34] T. J. E. Miller and M. McGlip, "Nonlinear theory of the switched reluctance motor for rapid computer-aided design," *IEE Proceedings*, pt. B, vol. 137, no. 6, pp. 337-347, Nov. 1990.

[35] A. D. Cheok and N. Ertugrul, "Computer based automated test measurement system for determining magnetization characteristics of switched reluctance motors," *IEEE Trans. on Instrumentation and Measurement*, vol. 50, no. 3, pp. 690-696, June 2001.

[36] J. F. Lindsay, R. Arumugam, and R. Krishnan, "Finite-element analysis characterization of a switched reluctance motor with multitooth per stator pole," *IEE Proceedings*, pt. B, vol. 133, no. 6, pp. 347-353, Nov. 1986.

[37] J. C. Lovatt and J. M. Stephenson, "Measurement of magnetic characteristics of switched reluctance motors," in *Proc. International Conf. on Electrical Machines*, Manchester, U.K., Sept. 1992, pp. 465-469.

[38] S. S. Murthy, B. Singh, and V. K. Sharma, "Finite element analysis to achieve optimum geometry of switched reluctance motor," in *Proc. IEEE International Conf. on Global Connectivity in Energy, Computer, Communication and Control*, New Delhi, India, Dec. 1998, vol. 2, pp. 414-418.

[39] N. Radimov, N. Ben-Hail, and R. Rabinovici, "Inductance measurements in switched reluctance machines," *IEEE Trans. on Magnetics*, vol. 41, no. 4, pp. 1296-1299, April 2005.

[40] J. Zhang and A. V. Radun, "A new method to measure the switched reluctance motor's flux," *IEEE Trans. on Industry Applications*, vol. 42, no. 5, pp. 1171-1176, Sept. 2006.

[41] Y. F. Tang and J. A. Kline, Sr., "Modeling and design optimization of switched reluctance machine by boundary element analysis and simulation," *IEEE Trans. on Energy Conversion*, vol. 11, no. 4, pp. 673-680, Dec. 1996.

[42] P. Zhang, P. A. Cassani, and S. S. Williamson, "A novel inductance profile measurement technique for switched reluctance machines," (accepted, under press) *IEEE Trans. on Industrial Electronics*, March 2010.

[43] I. Chindurza, D. G. Dorrell, and C. Cossar, "Assessing the core losses in switched reluctance machines," *IEEE Trans. on Magnetics*, vol. 41, no. 10, pp. 3907-3909, Oct. 2005.

[44] C. S. Edrington, M. Krishnamurthy, B. Fahimi, "An auto-calibrating inductance model for switched reluctance motor drives," *IEEE Trans. on Industrial Electronics*, vol. 54, no. 4, pp. 2165-2173, Aug. 2007.

[45] P. N. Materu and R. Krishnan, "Estimation of switched reluctance motor losses," *IEEE Trans. on Industry Applications*, vol. 28, no. 3, pp. 668-679, May 1992.

[46] P. Chancharoensook and M. F. Rahman, "Machine's characteristics identification: a preliminary study on direct torque control for switched reluctance motor drives," in *Proc. of the Australasian Universities Power Engineering Conf.*, Brisbane, Australia, Sept. 2000, pp. 132-137.

[47] V. Raulin, I. Husain, and A. Radun, "Modeling of losses in switched reluctance machines," *IEEE Trans. on Industry Applications*, vol. 40, no. 6, pp. 1560-1569, Nov. 2004.

[48] S. Inamura, T. Sakai, and K. Sawa, "A temperature rise analysis of switched reluctance motor due to the core and copper loss by FEM," *IEEE Trans. on Magnetics*, vol. 39, no. 3, pp. 1554-1557, May 2003.

[49] S. Balamurugan and P. Sumathi, "Analysis of temperature rise in switched reluctance motor due to the core and copper loss by coupled field finite element analysis," in *Proc. International Conf. on Power System Technology*, Singapore, Nov. 2004, vol. 1, pp. 630-634.

[50] M. V. K. Chari and P. P. Silvester, "Finite Elements in Electrical and Magnetic Field Problem," New York: John Wiley and Sons, 1980.

[51] M. Ehsani and B. Fahimi, "Elimination of position sensors in switched reluctance motor drives: state of the art and future trends," *IEEE Trans. on Industrial Electronics*, vol. 49, no. 1, pp.40-47, Feb. 2002.

[52] G. Suresh, B. Fahimi, K. M. Rahman, and M. Ehsani, "Analysis of amplitude modulation methods for sensorless SRM drives," in *Proc. IEEE Industrial Electronics Conf.*, Aachen, Germany, Sept. 1998, pp. 917-922.

[53] A. Medina and N. Garcia, "Newton methods for the fast computation of the periodic steady-state solution of systems with nonlinear and time-varying components," in *Proc. IEEE Power Engineering Society Summer Meeting*, July 1999, vol. 2, pp. 664-669.

[54] X. J. Tong, Y. P. Zhang, and F. F. Wu, "A decoupled semismooth Newton method for optimal power flow," *IEEE Power Engineering Society General Meeting*, July 2006, pp. 1-6.

[55] P. A. Cassani, P. Zhang, and S. S. Williamson, "A novel voltage-profiling method to minimize torque ripples in SRM based vehicle propulsion systems," in *Proc. 34th Annual Conf. of the IEEE Industrial Electronics Society*, Orlando, FL, Nov. 2008.

[56] Xilinx Company, "Virtex-II Pro and Virtex-II Pro X FPGA user guide," see: http://www.xilinx.com/support/documentation/user_guides/ug012.pdf.

[57] Xilinx Company, "Xilinx university program Virtex-II Pro development system-hardware reference manual," see: http://www.xilinx.com/univ/XUPV2P/Documentation/ug069.pdf.

[58] Xilinx Company, "Xilinx University Program Virtex-II Pro development system," see: http://www.xilinx.com/products/devkits/XUPV2P.htm.

[59] Xilinx Company, "System generator for DSP-getting started guide," see: http://www.xilinx.com/support/sw_manuals/sysgen_gs.pdf.

[60] Xilinx Company, "System generator for DSP-reference guide," see: http://www.xilinx.com/support/sw_manuals/sysgen_ref.pdf.

[61] Xilinx Company, "System generator for DSP-user guide," see: http://www.xilinx.com/support/sw_manuals/sysgen_user.pdf.

[62] P. Zhang and S. S. Williamson, "A novel FPGA based off-line control strategy for SRM integrated electric vehicle propulsion system," in *Proc. IEEE Canada Electrical Power and Energy Conf.*, Montreal, QC, Oct. 2009.

[63] P. Zhang and S. S. Williamson, "Novel control strategy design for switched reluctance motor based EV traction," in *Proc. IEEE Vehicle Power and Propulsion Conf.*, Dearborn, MI, Sept. 2009.

[64] P. Zhang and S. S. Williamson, "Design and implementation of a novel offline controller for a switched reluctance motor electric vehicle propulsion system," (submitted, under review) *IEEE Trans. on Vehicular Technology*, Feb. 2010.

[65] National Renewable Energy Laboratory (NREL), "Advanced Vehicle Simulator (ADVISOR) Documentation," see http://www.ctts.nrel.gov/analysis/advisor_doc.